

Spring 5-25-2019

Surface Engineering Solutions for Immersion Phase Change Cooling of Electronics

Brendon M. Doran

Follow this and additional works at: <https://digitalcommons.latech.edu/theses>

 Part of the [Electrical and Electronics Commons](#), [Heat Transfer, Combustion Commons](#), and the [Nanoscience and Nanotechnology Commons](#)

**SURFACE ENGINEERING SOLUTIONS FOR
IMMERSION PHASE CHANGE COOLING
OF ELECTRONICS**

by

Brendon M. Doran, B. S. Mechanical Engineering

A Thesis Presented in Partial Fulfillment
of the Requirements of the Degree
Master of Science

COLLEGE OF ENGINEERING AND SCIENCE
LOUISIANA TECH UNIVERSITY

May 2019

LOUISIANA TECH UNIVERSITY

GRADUATE SCHOOL

March 29, 2019

Date of thesis defense

We hereby recommend that the thesis prepared by

Brendon M. Doran

entitled **Surface Engineering Solutions for Immersion Phase Change**

Cooling of Electronics

be accepted in partial fulfillment of the requirements for the degree of

Master of Science in Engineering, Electrical Engineering Concentration

Dr. Arden Moore, Supervisor of Thesis Research

Dr. Chester Wilson,
Head of Electrical Engineering

Members of the Thesis Committee:

Dr. Arden Moore
Dr. Hisham Hegab
Dr. Sandra Zivanovic
Dr. Davis Harbour

Approved:

Hisham Hegab
Dean of Engineering & Science

Approved:

Ramu Ramachandran
Dean of the Graduate School

ABSTRACT

Micro- and nano-scale surface modifications have been a subject of great interest for enhancing the pool boiling heat transfer performance of immersion cooling systems due to their ability to augment surface area, improve wickability, and increase nucleation site density. However, many of the surface modification technologies that have been previously demonstrated show a lack of evidence concerning scalability for use at an industrial level. In this work, the pool boiling heat transfer performance of nanoporous anodic aluminum oxide (AAO) films, copper oxide (CuO) nanostructure coatings, and 1D roll-molded microfin arrays has been studied. Each of these technologies possess scalability in production, thus making them a subject of great interest to industry. To evaluate each surface modification technology, a custom pool boiling setup filled with 3M™ Novec™ HFE-7100 dielectric fluid was utilized. The pool boiling setup was autonomously operated by computer control using a custom LabVIEW™ program. Compared to natively oxidized aluminum samples, AAO samples showed improvements in surface area, but not in wickability or nucleation site density, allowing for the isolated study of the influence of increased surface area on pool boiling performance. Serving as an inverse analogue to nanoporous AAO films, protrusive CuO nanostructure coatings were shown to offer improvements in critical heat flux (CHF), wettability, and nucleation activity over their natively oxidized copper counterparts. At the micro-scale, 1D roll-molded microfin arrays were shown to have improved CHF and nucleation activity over

their planar counterparts. Following the initial pool boiling evaluation of each surface finish, the practical applicability of 1D roll-molded microfin arrays was demonstrated through a comparative study of cooling solutions for a field-programmable gate array (FPGA). In this study, the junction-to-ambient thermal resistance for an immersion cooling configuration that utilized a mounted 1D roll-molded microfin array surface was found to be lower than that of both a conventional forced-air cooling system and an immersion cooling configuration with no mounted surface. This finding highlights the significance of 1D roll-molded microfin array surfaces as an industrially acceptable means of improving the capabilities of immersion cooling systems.

APPROVAL FOR SCHOLARLY DISSEMINATION

The author grants to the Prescott Memorial Library of Louisiana Tech University the right to reproduce, by appropriate methods, upon request, any or all portions of this Thesis. It is understood that “proper request” consists of the agreement, on the part of the requesting party, that said reproduction is for his personal use and that subsequent reproduction will not occur without written approval of the author of this Thesis. Further, any portions of the Thesis used in books, papers, and other works must be appropriately referenced to this Thesis.

Finally, the author of this Thesis reserves the right to publish freely, in the literature, at any time, any or all portions of this Thesis.

Author _____

Date _____

DEDICATION

This thesis is dedicated to friends and family who have always pushed me to achieve more than what I was satisfied with, to educators who take a personal interest in the success of their students, and to the community of heat transfer engineers, scientists, and enthusiasts.

TABLE OF CONTENTS

ABSTRACT	iii
APPROVAL FOR SCHOLARLY DISSEMINATION	v
DEDICATION	vi
LIST OF FIGURES	ix
LIST OF TABLES	xii
ACKNOWLEDGMENTS	xiii
CHAPTER 1 INTRODUCTION.....	1
1.1 Immersion Cooling Overview	1
1.1.1 State of the Industry	1
1.1.2 Liquid-Vapor Phase Change Systems	2
1.2 Surface Modifications for Immersion Cooling Systems	5
1.2.1 Research Need.....	7
CHAPTER 2 METHODS	9
2.1 Preliminary Boiling Surface Evaluation	9
2.1.1 Pool Boiling Tank Configuration.....	9
2.1.2 Experimental Automation.....	11
2.1.3 Sample Preparation	14
2.2 Implementation of Boiling Surface on High-Power Electronic Device.....	15
2.2.1 Vertically-Oriented Immersion Tank	15
2.2.2 Use of an FPGA as a High-Power Electronic Device	16
CHAPTER 3 NANOSCALE SURFACE ENHANCEMENTS.....	19

3.1	Anodic Aluminum Oxide Nanoporous Surfaces	19
3.1.1	Surface Characterization.....	20
3.1.2	Pool Boiling Performance.....	22
3.1.3	Discussion of Results	24
3.2	Copper Oxide Nanostructure Surfaces	31
3.2.1	Surface Characterization.....	32
3.2.2	Pool Boiling Performance.....	34
3.2.3	Conclusions.....	36
CHAPTER 4 HIGH-THROUGHPUT 1D ROLL-MOLDED MICROFIN ARRAY SURFACES		38
4.1	Preliminary Surface Evaluation	39
4.1.1	Pool Boiling Performance.....	39
4.1.2	Discussion of Results	42
4.2	Practical Evaluation of Enhanced Surfaces for Immersion Cooling Systems...45	
4.2.1	Discussion of Results	48
4.2.2	Conclusions.....	49
CHAPTER 5 CONCLUSIONS AND FUTURE WORK.....		51
5.1	Conclusions	51
5.2	Future Work.....	52
APPENDIX A	Important Definitions and Terminology.....	54
APPENDIX B	Scalable Clock Divider Code.....	56
APPENDIX C	Uncertainty Calculations	58
APPENDIX D	AAO Surface Area Calculations	59
BIBLIOGRAPHY		60

LIST OF FIGURES

Figure 1-1: Fluid cycle in phase change immersion cooling system.	3
Figure 2-1: Schematic representation of pool boiling tank setup used for sample evaluation with. Here, the stage is shown to be in the horizontal orientation.	10
Figure 2-2: Simplified block diagram representation of LabVIEW program used for sample evaluation.	12
Figure 2-3: LabVIEW™ front panel display for pool boiling experiment.....	13
Figure 2-4: Left: Render of preliminary vertical boiling tank model generated in Solidworks™. Right: Fully assembled vertical boiling tank.	16
Figure 2-5: Schematic for clock divider circuit used to produce thermal loads on the FPGA.	17
Figure 2-6: Stock forced-air cooling system for the Genesys 2 development board.	18
Figure 3-1: (a) Schematic representation of anodization setup; (b) image of AAO surface produced by the two-step anodization process. Both images were provided courtesy of the Wen Jin Meng group from LSU.	20
Figure 3-2: (a) Typical plane-view of AAO surface; (b) typical cross-sectional view of epitaxial AAO layer. Both images were provided courtesy of the Wen Jin Meng group from LSU.	21
Figure 3-3: Static contact angle measurements for DI water on (a) natively oxidized and (b) nanoporous AAO aluminum surfaces.....	22
Figure 3-4: Pool boiling performance of natively oxidized and AAO aluminum samples in the horizontal stage orientation.	23
Figure 3-5: Pool boiling performance of natively oxidized and AAO aluminum samples in the vertical stage orientation.	24
Figure 3-6: Percent sidewall wetting as a function of (a) surface tension for both water and Novec™ HFE-7100 and (b) pore diameter. The inset of (b) schematically demonstrates the force balance described by the Ran model.....	26

Figure 3-7: Adjusted pool boiling performance for samples in the horizontal stage orientation. Superheat values for AAO data points have been shifted down by the AAO/fluid thermal resistance-heat flux product.....	28
Figure 3-8: Still images taken at the onset of nucleate boiling ($\Delta T = \sim 0-5$ K) for (a) native oxide and (b) AAO samples in the horizontal orientation.....	29
Figure 3-9: Size range of active nucleation sites predicted by the Hsu model for Novec TM HFE-7100 compared to the size range of nanopore radii for samples studied in this work.....	30
Figure 3-10: Left to right: (a) as-received copper square with native oxide, (b) sample after sanding and HCl dip, (c) nanostructure-coated sample after second oxidation cycle.	31
Figure 3-11: SEM images depicting CuO nanostructures. Image (a) shows multiple nanostructures while (b) shows an individual nanostructure.	32
Figure 3-12: EDS scan of CuO nanostructure coated sample surface.....	33
Figure 3-13: Static contact angle measurement for DI water on (a) natively oxidized and (b) CuO nanostructure coated copper surfaces.	34
Figure 3-14: Pool boiling performance of natively oxidized and CuO nanostructure coated copper samples.	35
Figure 3-15: Still images taken at 40 K of superheat for (a) native oxide and (b) CuO nanostructure coated samples in the horizontal orientation.	36
Figure 4-1: Cross-sectional images depicting fin geometry for microfin arrays generated using compression forces of (a) 5000 lbf, (b) 15000 lbf, and (c) 23000 lbf.	39
Figure 4-2: Pool boiling performance of 1D roll-molded microfin array samples and planar control samples in the horizontal stage orientation.....	40
Figure 4-3: Pool boiling performance of 1D roll-molded microfin array samples and planar control samples in the vertical stage orientation.....	41
Figure 4-4: Representative still image depicting observed bubble formation behavior. Some of the initially formed vapor bubbles are identified.	43
Figure 4-5: Still images taken at $\sim 30-40$ K of superheat for (a) planar control, (b) 5000 lbf roll-molded, (c) 15000 lbf roll-molded, and (d) 23000 lbf roll-molded samples.....	45
Figure 4-6: Performance summary of cooling solutions for managing the thermal loads produced by the FPGA.	47

Figure 4-7: Still image taken during immersion cooling testing of the FPGA depicting nucleation on the surface of the roll-molded microfin heat transfer surface.....49

LIST OF TABLES

Table 1-1: Thermophysical properties of two common dielectric fluids compared with water, adapted from [19].....	5
---	---

ACKNOWLEDGMENTS

This work was supported through funding from the National Science Foundation through cooperative agreement OIA-1541079 and the Louisiana Board of Regents. A special thanks is given to Dr. Wen Jin Meng and Bin Zhang from Louisiana State University, Dr. Patrick Mensah's group from Southern University, and Luke Hansen for their collaboration throughout this project. Additionally, a great gratitude is offered to John Serio and Joey Higuera for their technical assistance in developing the vertical immersion cooling experimental setup used for this work and to Tyler Spence for motivation and guidance throughout this entire process. Lastly, I would like to most sincerely thank my advisor, Dr. Arden Moore, for his continued advice and guidance throughout the past four years that have made the realization of this project possible.

CHAPTER 1

INTRODUCTION

1.1 Immersion Cooling Overview

1.1.1 State of the Industry

High-powered electronic devices are widespread in use and their performance is an ever-increasing demand. To facilitate this demand, improved thermal management solutions are constantly in development to manage the heat generated by newer and more powerful electronic devices and systems. Historically, forced-air systems have been the standard for cooling datacenters and High-Performance Computers (HPCs)[1]. However, the cost to operate forced-air systems has increased greatly as the thermal loads they manage have increased. In 2017, the United States Department of Energy (DoE) reported that of the estimated 70 billion kWh of power consumed by datacenters in the United States, approximately 33% of the power consumed for “midtier” and “high-end” data centers was dedicated solely to cooling solutions[2]. Due to these high operating costs, industry is now considering direct immersion cooling solutions which have the potential to offer greater heat transfer efficiencies than forced-air systems[3]. Forced-air cooling systems have typical convection heat transfer coefficients in the range of 25-250 $\text{W m}^{-2} \text{K}^{-1}$ while immersion cooling systems can have much higher effective convection heat transfer coefficients in the range of 50-1,000 $\text{W m}^{-2} \text{K}^{-1}$ for single phase systems and 2,500-100,000 $\text{W m}^{-2} \text{K}^{-1}$ for phase change systems[4]. This vast difference in heat transfer coefficients

enables phase change immersion cooling systems to greatly expand the thermal management capabilities of datacenters and HPCs over forced-air systems.

Previously, direct immersion cooling systems were not seen as viable for several reasons, including a lack of environmentally safe working fluids, the inability to submerge computers due to their size, and the frequent maintenance needs of computers at the time[3]. However, with the rise of environmentally friendly thermally-stable fluorinated fluids and the reduced size and maintenance of modern computers, the realization of effective direct immersion cooling systems is possible. Several modern datacenters and HPCs now utilize fluorinated fluid-driven direct immersion cooling systems to manage the large thermal loads generated by their usage[5–7]. These immersion cooling systems appear in both natural and forced convection variants and can be single-phase or two-phase. In single phase systems, the temperature and pressure of the working fluid is maintained below the boiling point, so the fluid remains in a liquid state. In two-phase systems, the temperature and pressure of the fluid exceed the boiling point, causing the fluid to undergo phase change and convert to a vapor.

1.1.2 Liquid-Vapor Phase Change Systems

When compared to single-phase immersion cooling systems, two-phase liquid-vapor immersion cooling systems allow for increased heat transfer rates by capitalizing on the latent energy required to change the state of the working fluid from a liquid to a vapor. By leveraging the latent heat of vaporization, large amounts of heat can be transferred from the heat source to the working fluid without requiring a large temperature difference between the fluid and heat transfer surface. Once the working fluid has been converted to

vapor, it escapes the reservoir and interacts with a condenser to be converted back into a liquid and return to the reservoir. A depiction of this process is shown in **Figure 1-1**.

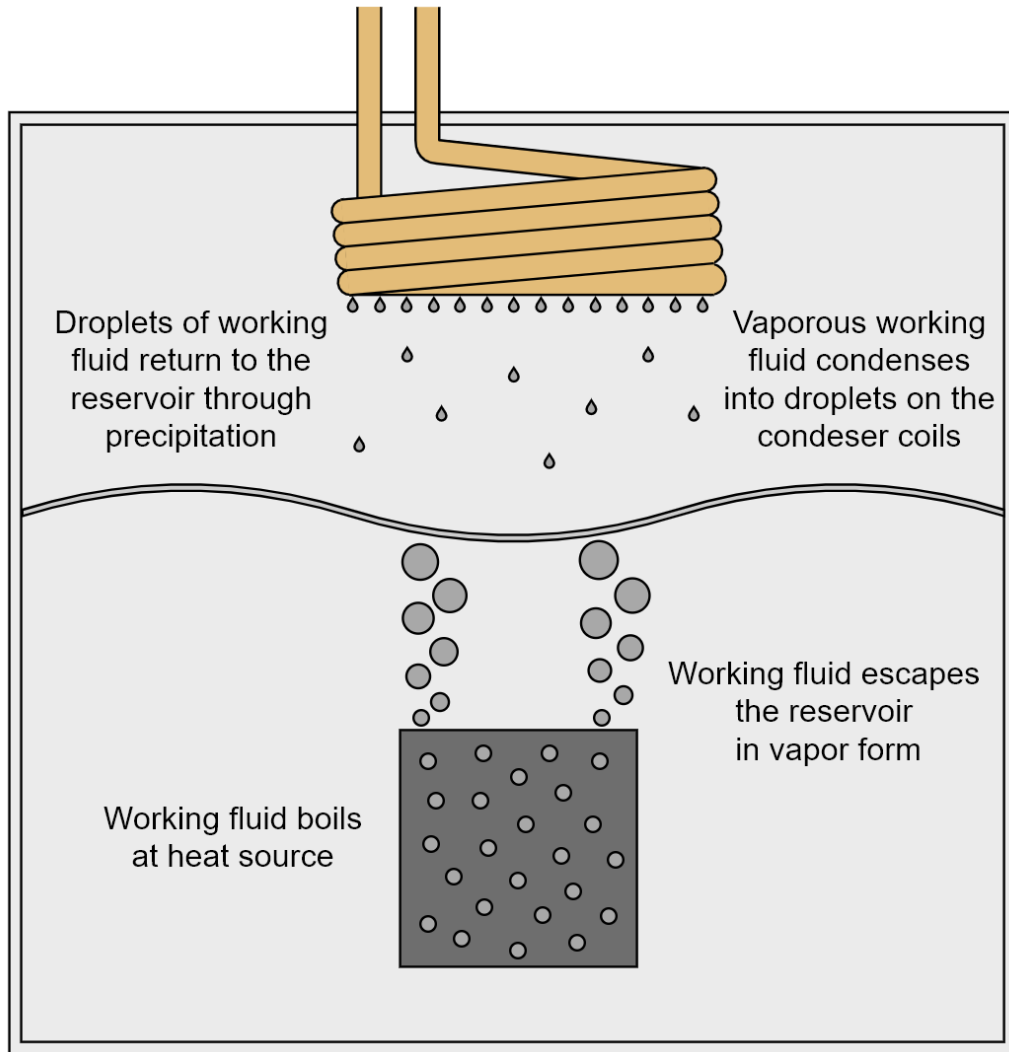


Figure 1-1: Fluid cycle in phase change immersion cooling system.

In the case of a pool boiling system, the highest heat transfer values are found at the end of the nucleate boiling regime, just before transitioning to the film boiling regime [4]. During this time, buoyancy-driven natural convection operates at a peak due to the large difference in densities between surface fluid and bulk fluid. This difference in densities allows hot fluid to quickly escape from the high temperature region near the

sample surface to the lower temperature bulk fluid. The orientation of the heat transfer surface influences the ability of the surface to transfer heat through boiling. Literature has shown that the boiling heat flux of a surface decreases as the orientation of the surface is shifted from horizontally oriented to vertically oriented[8,9].

Additionally, the working fluid used in a pool boiling system contributes to the ability of the system to transfer heat effectively. In a majority of literature related to surface enhancement for pool boiling systems, water was used as the working fluid of choice due to its industrial significance[10–13]. However, when developing pool boiling solutions for use in the immersion cooling of electronics, the compatibility of heat transfer solutions with modern dielectric fluids, such as the 3M™ Fluorinert™ and Novec™ product lines, is of great importance. As a result of growing interest in immersion cooling solutions for electronics, motivation for studying the behavior of boiling surfaces in dielectric fluids has increased in recent years[14–18]. The thermophysical properties of modern dielectric fluids differ significantly from those of water, with fluorinated dielectric fluids having much lower boiling points, surface tensions, and latent heats of vaporization than water as shown in **Table 1-1**[19]. These differences in fluid properties mandate different design constraints when developing boiling surfaces for use in dielectric fluids instead of water. Of these differences, the surface tension disparity between the dielectric fluids and water is of particular importance since surface tension of the fluid influences the bubbling behavior through changes in bubble diameter and departure frequency.

Table 1-1: Thermophysical properties of two common dielectric fluids compared with water, adapted from [19].

	Fluorinert™ FC-72	Novec™ HFE-7100	Water
Boiling point (°C)	56	61	100
Liquid density (kg m ⁻³)	1680	1510	997
Liquid dynamic viscosity (kg m ⁻¹ s ⁻¹)	6.4x10 ⁻⁴	5.8x10 ⁻⁴	8.9x10 ⁻⁴
Liquid specific heat (J kg ⁻¹ K ⁻¹)	1100	1183	4182
Liquid thermal conductivity (W m ⁻¹ K ⁻¹)	0.057	0.069	0.61
Latent heat of vaporization (kJ kg ⁻¹)	88	112	2257
Liquid surface tension (mN m ⁻¹)	10	13.6	72

1.2 Surface Modifications for Immersion Cooling Systems

In the pursuit of improving the performance of immersion liquid-vapor two-phase systems, the usage of specially engineered boiling surfaces has been investigated. By modifying boiling surfaces to tailor the interfacial interactions between the working fluid and surface, the ability of the fluid to efficiently remove heat from the surface and undergo phase change can be improved.

In the past twenty years, much of the research on boiling surface enhancement has been focused on micro- and nano- scale structures as a means of improving the boiling heat transfer capabilities of heat transfer surfaces by increasing surface area, controlling wettability, improving wickability, and increasing nucleation site density[12,13,26–33,14,15,20–25]. While increasing surface area is a well-studied means of improving

convection heat transfer at the meso scale, much work has been done in recent years to investigate the effects of micro scale surface enhancements on convection heat transfer in single- and two-phase systems. By leveraging the capabilities of modern micromanufacturing techniques, surface features such as microchannels and microfin arrays have been realizable with high throughput[34]. These surface structures enhance the effective heat transfer surface area of the boiling surface and have been shown to improve boiling performance in both water and dielectric fluids[26,27,31]. Control of surface wettability has been found to affect the boiling capabilities of surfaces for both high and low heat fluxes. For lower heat fluxes, highly hydrophobic surfaces have been shown to initiate nucleate boiling at superheats two orders of magnitude lower than their hydrophilic counterparts[28]. Due to this low threshold to boiling incipience, hydrophobic surfaces can obtain high heat transfer coefficient (HTC) values at relatively low surface heat fluxes. At higher heat fluxes, highly hydrophilic surfaces delay the onset of film boiling due to their ability to rapidly rewet the surface, leading to increases in CHF[28,32]. This tradeoff presents a dilemma where hydrophobic surfaces excel in lower heat flux applications while hydrophilic surfaces excel in higher heat flux applications.

The wickability of a surface has also been shown to play an important role in enhancing CHF. For hierarchical surfaces generated using Tobacco mosaic virus templating, Rahman et al. showed enhancements in CHF that correlated with the increase in wickability of the surface[29]. Additionally, Shim et al. demonstrated improvements in CHF for a surface covered in aligned silicon nanowires when compared to a surface covered in randomly-grouped nanowires, attributing the improved CHF to the increased wicking capability of the aligned nanowire surface[33]. In conjunction with surface

wettability and wickability, nucleation site density plays a key role in the boiling heat transfer capabilities of a surface. Balakrishnan et al. and Jones et al. have shown correlations between increased nucleation site density and improved boiling heat flux on stainless steel and aluminum surfaces in water and FluorinertTM FC-77 where nucleation site density was controlled by varying surface roughness[11,22]. Additionally, many studies that utilize micro- and nanoporous surface structures to increase nucleation site density note improvements in boiling heat flux when compared to their plain counterparts[14,15,21,23]. While wettability, wickability, and nucleation site density all individually contribute to pool boiling performance, technologies seeking to improve boiling capabilities will typically utilize all three of these phenomena simultaneously due to their tightly interrelated nature.

This work seeks to evaluate the effects of engineered surface finishes on the performance of immersion two-phase cooling solutions for electronics while focusing on commercial and industrial applications. In addition, high performance evaluation techniques which mimic realistic industrial environments while also allowing for repeatable, automated experiment control and data acquisition will be designed, developed, and implemented.

1.2.1 Research Need

While engineered surfaces for improved boiling are an area of intense research focus, there are still some technology gaps in the field that are targeted in this work. One such technology gap is the development of multiscale engineered surfaces for enhanced boiling performance. Multiscale surfaces utilize macro-, micro-, and nanoscale features such as microscale fins, anodized nanopores, and surface-mounted nanowires to tailor the

interfacial interactions between the surface and the surrounding fluid. To gain wide-spread adoption, any such surface should be realized over surfaces on the order of square centimeters or more at low cost, a requirement which represents a barrier to many current nanomaterials-based coatings. Additionally, understanding the mechanisms behind the boiling improvements offered by multiscale surface structures has remained a scientific challenge. While it is understood that applying multiscale surface structures to boiling surfaces can improve the boiling performance by increasing the surface area, wickability, and nucleation site density; isolating the individual contributions of each of these three components has proven to be difficult. By addressing these technology gaps, new surface technologies can be developed that further push the performance of engineered surfaces for boiling heat transfer scenarios.

Another technology gap in this field of research is engineered surface solutions for commercial electronics immersed in two-phase cooling systems. This technology gap serves as a bridge between experimental and practical solutions for phase change cooling of electronics as it applies experimental surface engineering designs to a real-life scenario. Many studies have investigated pool boiling scenarios while simulating the behavior of immersed electronics by using simple heated surfaces, this work will differ by investigating the performance of an actual high-powered electronic device with mounted engineered surfaces in a phase change cooling scenario. By addressing this technology gap, previous knowledge from experimental findings can be applied to practical engineered surface designs to be used in phase change cooling systems.

CHAPTER 2

METHODS

2.1 Preliminary Boiling Surface Evaluation

2.1.1 Pool Boiling Tank Configuration

Samples were evaluated using the pool boiling tank setup shown in **Figure 2-1**. The pool boiling tank is composed of mirror-finish 316 stainless steel plates and contains the sample stage, working fluid (3M™ Novec™ HFE-7100), cooling coil, and condenser coil. The sample stage is constructed from a polytetrafluoroethylene (PTFE) base, nickel-chromium (nichrome) wire heater, and a copper heat spreader block. The copper heat spreader has two channels machined into its upper surface to accommodate two insulated K-type thermocouples that are used to monitor temperature on the backside of the sample during testing. The thermocouples were manufactured by OMEGA® and have an operating range of 0 °C to 200 °C with a reported maximum error of the greatest value between ± 2.2 °C or .75% of the read value in Celsius. The nichrome wire heater is adhered to the back of the copper heat spreader with OMEGABOND™ 200 thermally conductive epoxy to minimize the thermal resistance present between the heater and the heat spreader. A second piece of PTFE with sample space cutout surrounds the sample base and resides on top of the main PTFE block. All seams on the stage are sealed with room-temperature vulcanizing (RTV) silicone to prevent unwanted heat transfer caused by fluid ingress into the stage.

The stage is suspended from the lid by two nylon dowels that connect on either side of the stage; these dowels allow for height and orientation adjustment of the stage.

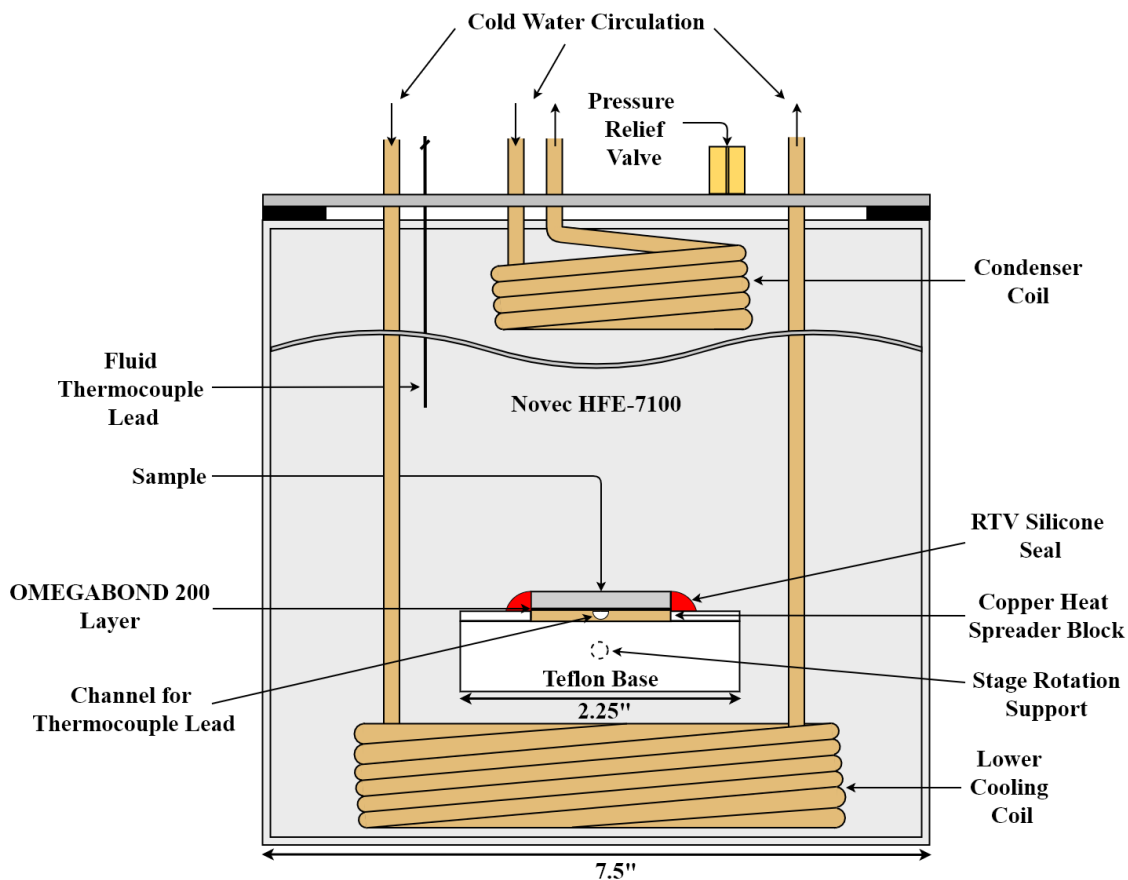


Figure 2-1: Schematic representation of pool boiling tank setup used for sample evaluation with. Here, the stage is shown to be in the horizontal orientation.

To test samples, the pool boiling tank was filled with Novec™ HFE-7100 dielectric fluid and the stage with the mounted sample was submerged. While the experimental setup was running, a liquid-to-air heat exchanger cycled water through a pair of cooling coils located at the top and bottom of the boiling rig, respectively. The lower cooling coil maintained the pool at a constant temperature, while the upper cooling coil facilitated condensation of the coolant vapor, thus maintaining a constant liquid level throughout the experiment. Passing through the lid of the tank is a pressure relief valve that was used to

maintain the inside of the tank at 1 atm of pressure while the tank was sealed during testing. An additional K-type thermocouple passes through the lid of the tank and was used to monitor the temperature of the fluid bath. Three of the four walls of the tank have circular hole cutouts with polycarbonate windows mounted in place to allow for viewing the inside of the tank while the tank is sealed. During testing, a camera was mounted outside of one of the windows to allow for image and video capture of the stage and sample. Employing a 1D planar wall conduction model to account for thermal conduction to the surroundings through the stage and power leads, a heat flux uncertainty value of $\pm \sim 2.3\%$ was obtained for this experimental setup; details of the calculations used to obtain this uncertainty value are shown in **Appendix B**.

2.1.2 Experimental Automation

To ensure consistency and repeatability, the pool boiling experiment and associated data acquisition were operated via automated computer control using LabVIEW™, WinDaq™, and IC Capture™. A custom LabVIEW™ program initiated the experiment by setting the heater power supply voltage to a starting value of 5 V. The program then began to monitor temperature data from the two thermocouples mounted to the backside of the sample and the third thermocouple immersed in the working fluid bath. As the temperature values were read, the program recorded the raw reported temperature values for all three thermocouples and the associated time stamp. The temperature values from the two stage-mounted thermocouples were averaged and the resulting value was stored to a buffer. The buffer maintained the five most recent average temperature values and their respective time stamps and performed a linear regression on the values, returning the resulting slope value. The returned slope value was then compared to a convergence parameter of $.01 \text{ K s}^{-1}$. When

the slope value fell below the convergence parameter, the program flagged the temperature of the sample as having reached steady-state. Once the temperature of the sample reached steady-state, the LabVIEW™ program switched off the power supply, incremented the power supply voltage by +2 V, switched the power supply back on, and repeated the monitoring process until another steady state flag was issued. The monitoring and incrementing process was repeated until the average sample temperature reached 100 °C where the program flagged the experiment as complete, causing the program to terminate.

Figure 2-2 shows a block diagram for the LabVIEW program.

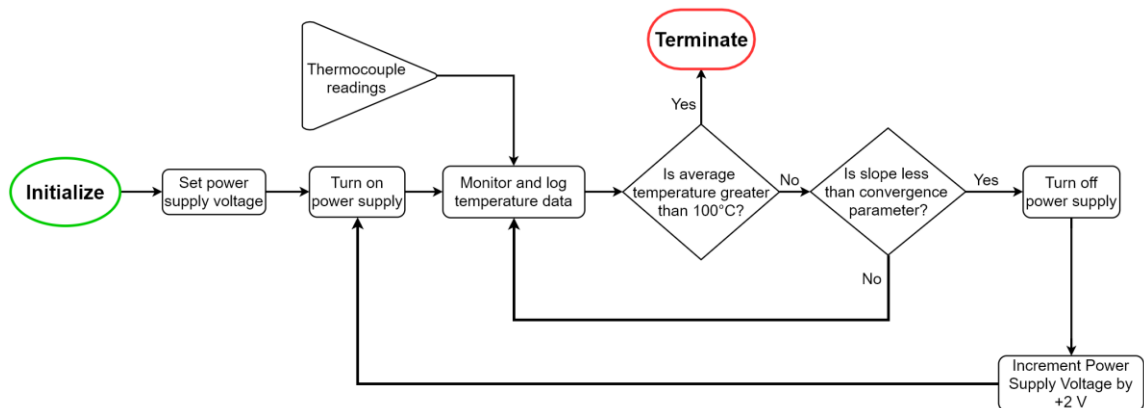


Figure 2-2: Simplified block diagram representation of LabVIEW program used for sample evaluation.

While the LabVIEW™ program was running, a front panel display was configured to provide the user with vital information for monitoring the status of the experiment. Key parts of the front panel display included the temperature graph, power supply readings, thermocouple temperature readings, and slope calculation. On the temperature graph, the temperatures of both sample-mounted thermocouples and the fluid bath thermocouple were plotted against time. A sample front panel display is shown in **Figure 2-3**. In addition to providing information to the user, the front panel display also allowed the user to tweak

experimental parameters to alter the conditions of the experiment as needed. Parameters that could be altered included the starting voltage, incremental voltage step size, convergence parameter, and maximum allowable current and voltage for the power supply.

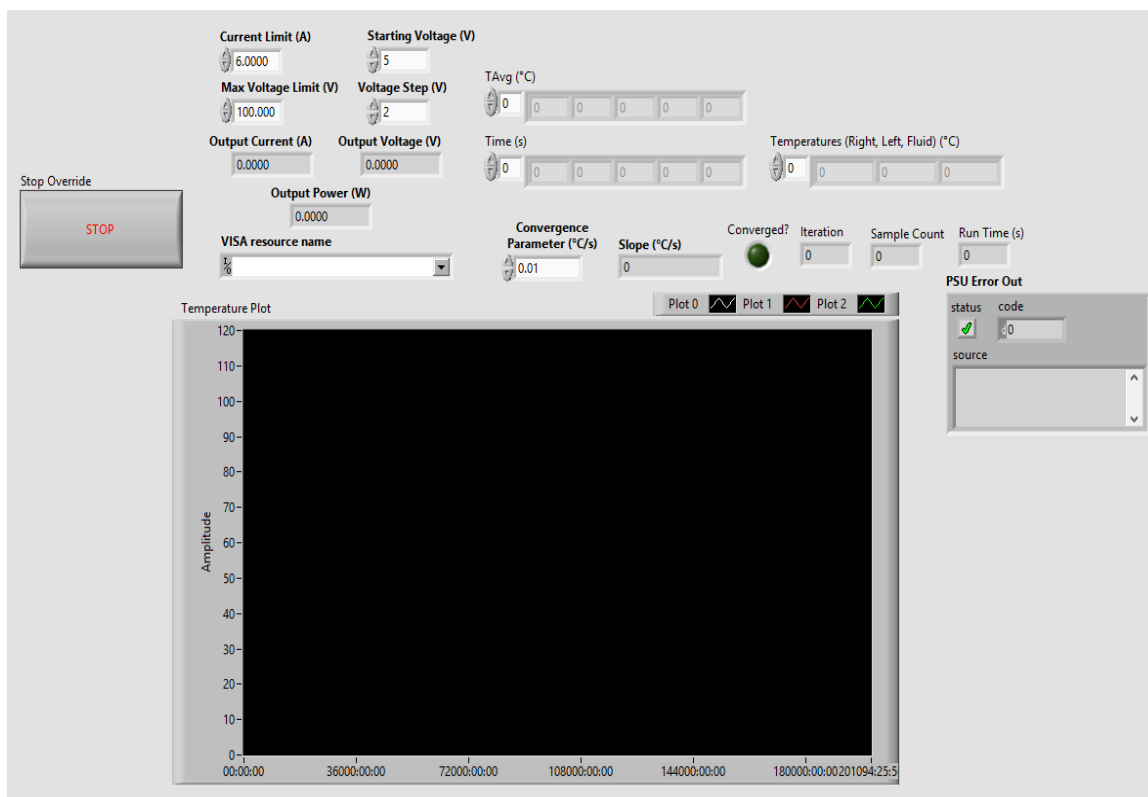


Figure 2-3: LabVIEW™ front panel display for pool boiling experiment.

Aside from the LabVIEW™ program, a WinDaq™ instance was used to log voltage and current readings from the heater circuit to determine the power dissipation of the nichrome wire. The WinDaq™ instance sampled voltage values across both the nichrome heater and a sense resistor. The sense resistor had a resistance of $1\ \Omega$, so the voltage value measured across the resistor was equivalent to the current flowing through it. Also running during testing was an instance of IC Capture™. The IC Capture™ instance was used to monitor the camera mounted outside of the boiling tank and take video and

still images of the sample during testing. An automated sequence feature within IC Capture™ was utilized to take still images of the sample every 60 seconds while the experiment was running.

2.1.3 Sample Preparation

Before testing, samples underwent a standardized preparation procedure to ensure sample to sample consistency. Before mounting the sample to the stage, the stage was first cleaned and prepared for mounting. The copper heat block was first scraped clean of any residual OMEGABOND™ from previous experiments. The heat block was then sanded and wiped down to ensure an even and clean surface. In a disposable dish, the two-part OMEGABOND™ was mixed at a 10:1 ratio of resin to catalyst. After mixing, the OMEGABOND™ was applied to the surface of the copper heat block and the sample was carefully placed on top of the epoxy layer. The two stage thermocouples were then inserted into the channels on either side of the sample at the seam between the sample and copper heat block. After the thermocouples were inserted, the sample was depressed to force out excess OMEGABOND™ and ensure good contact between the epoxy and both surfaces. Excess OMEGABOND™ was removed from the seam between the heat block and sample and the stage was then left for two days to allow the epoxy to cure. After two days, a silicone RTV sealant was applied to the seam between the copper heat block and sample and the stage was left for an additional day to allow the silicone RTV to cure. After one day, the samples were ready to be evaluated in the pool boiling tank.

2.2 Implementation of Boiling Surface on High-Power Electronic Device

2.2.1 Vertically-Oriented Immersion Tank

A passively cooled, vertically-oriented immersion cooling tank was designed and fabricated to be used in demonstrating the practical effectiveness of the immersion cooling solutions developed in this work. A 3D computer model of the tank is shown in **Figure 2-4**. The tank is composed of a custom-machined aluminum unibody frame covered on either side by clear polycarbonate panels and on top by an aluminum lid. It is assembled using bolted fasteners and utilizes custom cut neoprene gaskets at each interface to seal the tank. Two cable routing holes are cut from the lid and sealed with rubber pass-through gaskets to allow for power and data lines to be run into the tank while maintaining a liquid-tight seal. Attached to the bottom of the tank is a two-position globe valve that allows the tank to be easily drained of fluid. By leveraging the high thermal conductivity and surface area of the aluminum frame, the tank is able to maintain the temperature of the internal working fluid by passively transferring heat to the surroundings for the board power levels tested here. A single vertical rack is used for mounting electronic devices during testing to simulate the normal operating conditions for a commercial immersion cooling system[5]. Due to its lightweight and compact nature, the tank acts as a portable evaluation platform with the ability to be carried by the handle mounted atop the lid. It can also be used for demonstration, recruitment, and outreach activities.

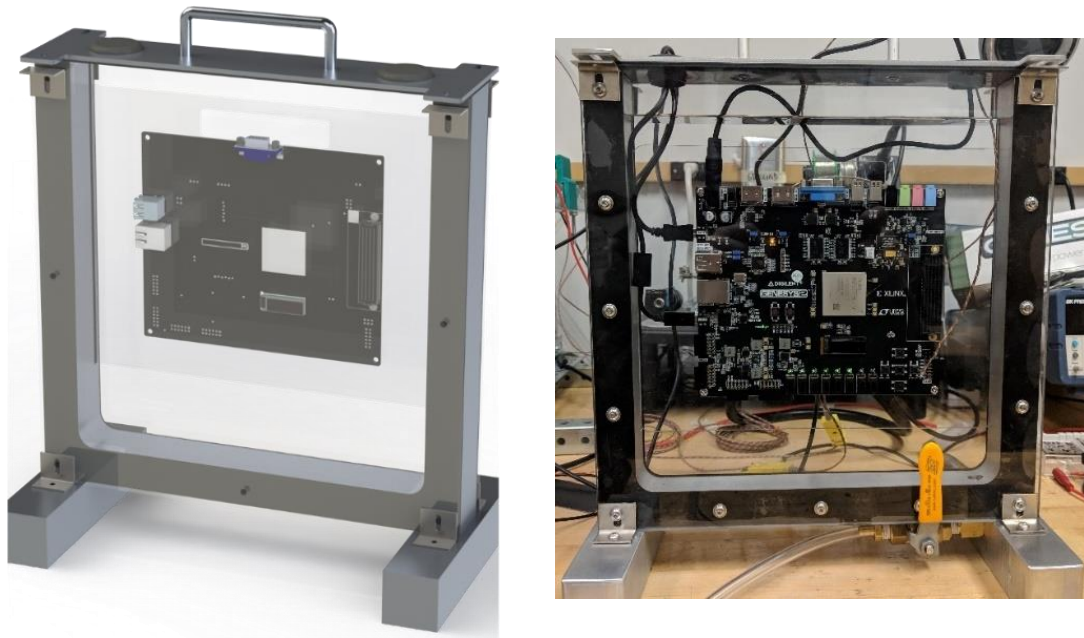


Figure 2-4: Left: Render of preliminary vertical boiling tank model generated in Solidworks™. Right: Fully assembled vertical boiling tank.

2.2.2 Use of an FPGA as a High-Power Electronic Device

In this work, a Xilinx™ Kintex™-7 field-programmable gate array (FPGA) was used to produce thermal loads for each cooling system to manage. The FPGA was mounted to a Digilent™ Genesys 2 development board that allowed for interfacing with the FPGA. To produce thermal loading, the FPGA was populated with clock divider circuits using Vivado Design Suite™. A single instance of the clock divider circuit used in this work is shown in **Figure 2-5**. Clock dividers were chosen for their simplicity, scalability, and synchronous nature. Because clock dividers are synchronous circuits, the power draw of the FPGA could be controlled by both the number of clock divider circuits implemented in the FPGA and the frequency that the clock divider circuits were driven at.

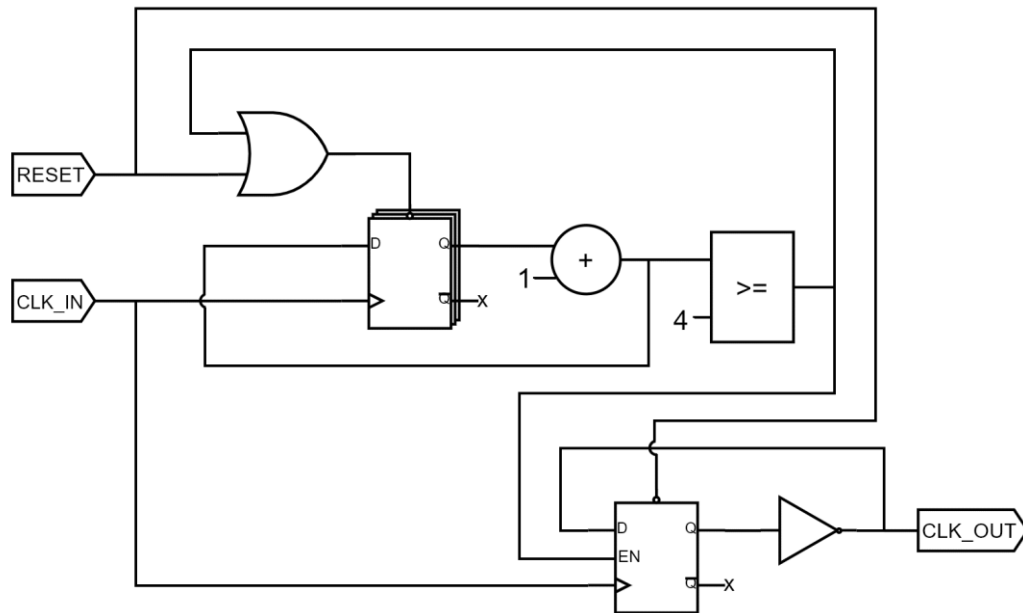


Figure 2-5: Schematic for clock divider circuit used to produce thermal loads on the FPGA.

In addition to clock divider circuits, a Microblaze™ soft processor core was instantiated on the FPGA to measure and report power and temperature data for the FPGA. Power draw data was read from several on-board sensors connected to each of the power rails while temperature data was read from a temperature sensor within the FPGA. Measured values for power and temperature were reported back using a universal asynchronous receive/transmit (UART) connection. All external inputs and outputs (I/O) besides communication hardware and onboard light-emitting diodes (LEDs) were disabled to prevent additional power draw outside the FPGA. The onboard LEDs were used to provide hardware connections to the outputs of the clock divider circuits to prevent the software from removing the clock divider circuits during optimization.

Using this setup, the FPGA was exercised at increasing power levels for three cooling configurations: i) forced air convection via the stock fan-sink, ii) liquid immersion cooling with the fan sink removed, and iii) liquid immersion cooling with a custom roll-molded microfin array as will be described further in later chapters. This was done so the thermal management performance of the three cooling approaches could be quantitatively compared. The stock forced air system shown in **Figure 2-6** consisted of a 1.25 x 1.25-inch square pin-fin heat sink, fan, and thermal interface material (TIM) used to connect the heat sink to the integrated heat spreader (IHS) of the FPGA. For the immersion cooling configurations, the vertically-oriented tank was filled with Novec™ HFE-7100 and the development board was submerged with and without an engineered heat transfer surface mounted to the IHS.



Figure 2-6: Stock forced-air cooling system for the Genesys 2 development board.

CHAPTER 3

NANOSCALE SURFACE ENHANCEMENTS

3.1 Anodic Aluminum Oxide Nanoporous Surfaces

The boiling heat transfer effectiveness of nanoporous anodic aluminum oxide (AAO) coated surfaces as an inverse analogue to nanowire coated surfaces was investigated. The AAO samples studied in this work were obtained through a collaboration with the Wen Jin Meng group from Louisiana State University (LSU). To produce the AAO nanoporous surfaces, 1-inch x 1-inch Al 1100 aluminum squares were anodized using a two-step process. Before anodization, the samples were first sanded and polished using silicon carbide (SiC) sanding paper. Following sanding and polishing, samples were annealed and cleaned to ensure consistent microstructures and starting surface conditions. Immediately prior to anodization, samples were submerged into a 1M sodium hydroxide solution to remove pre-existing oxide layers. Both anodization steps were performed using a platinum foil cathode and 0.3M oxalic acid electrolyte solution at 20 °C in a custom-built anodization setup shown in schematically in **Figure 3-1(a)**. The first anodization step was performed for 5 minutes at a biasing voltage of 30V. Following the first anodization step, samples were submerged in a 1M sodium hydroxide solution for 5 minutes to etch away the recently formed aluminum oxide layer. The second anodization step was performed for 45 minutes at a biasing voltage of 40V. Following the second anodization step, samples were submerged in a 5 wt.% phosphoric acid solution at room temperature for 20 minutes

to open pores that were blocked during the anodization process. Samples were then rinsed with deionized (DI) water and dried. The resulting surface produced by the anodization process is shown in **Figure 3-1(b)**.

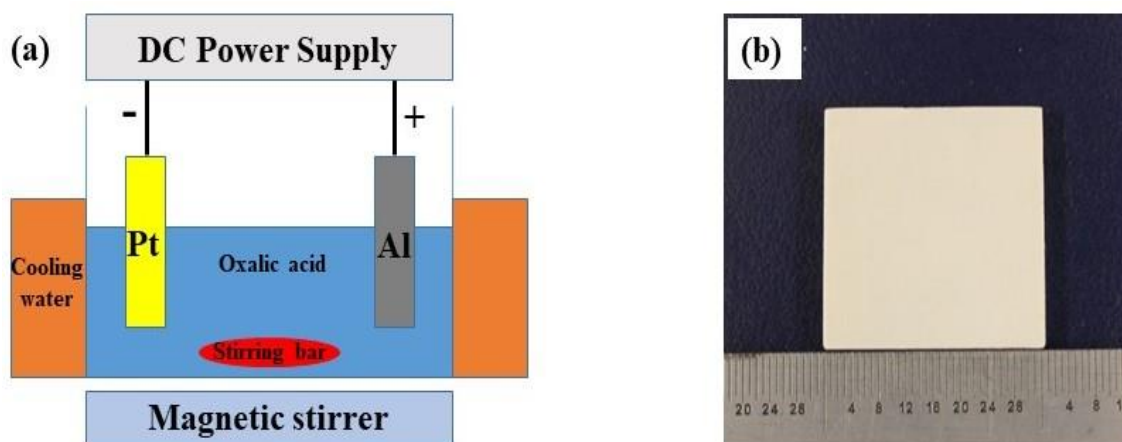


Figure 3-1: (a) Schematic representation of anodization setup; (b) image of AAO surface produced by the two-step anodization process. Both images were provided courtesy of the Wen Jin Meng group from LSU.

3.1.1 Surface Characterization

Following anodization, samples were inspected using a FEI Quanta3D FEG Dual-Beam scanning electron microscope/focused ion beam (SEM/FIB). SEM imaging was used to provide a plane-view of samples while FIB imaging was used to provide cross-sectional views of the epitaxial AAO layer, as shown in **Figure 3-2**. Using the SEM, pore diameters were measured to range from approximately 40 nm to 140 nm with an average pore diameter of 80 nm. Using the FIB, average AAO layer thickness was measured to be approximately 14 μm .

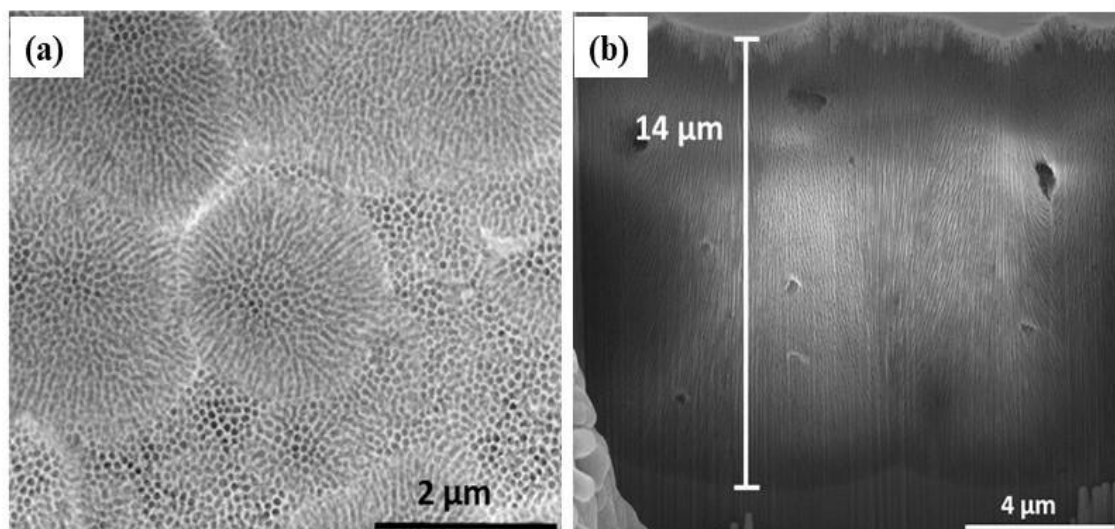


Figure 3-2: (a) Typical plane-view of AAO surface; (b) typical cross-sectional view of epitaxial AAO layer. Both images were provided courtesy of the Wen Jin Meng group from LSU.

To understand how the nanoporous AAO layer would affect the wetting behavior of the surfaces, the static contact angles for both natively oxidized and AAO samples were measured. Initial attempts to measure the static contact angle using NovecTM HFE-7100 were unsuccessful due to the low surface tension of the fluid. As a result, all contact angles measured for both natively oxidized and AAO surfaces fell below 5 °. Following this, further contact angle measurements were performed using deionized water and are shown in **Figure 3-3**. For natively oxidized aluminum samples, the static contact angle was measured to be 81.1 degrees while for AAO-coated aluminum surfaces, the contact angle was measured to be 66.6 degrees. These contact angle values agree with those presented in literature for AAO films with 70-80 nm pore diameters and suggest that the AAO surfaces have slightly better surface wetting characteristics than their natively oxidized counterparts[21].

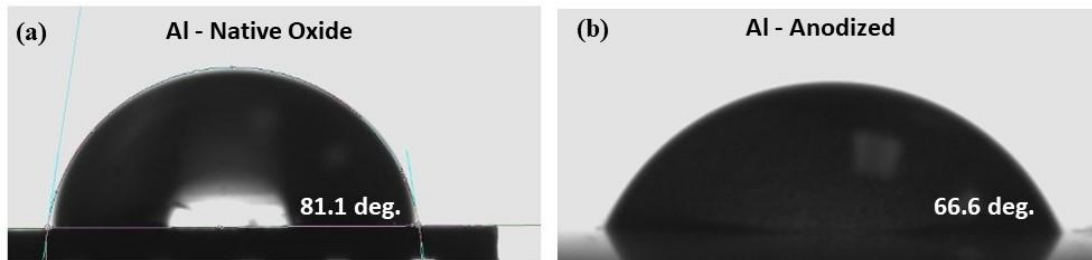


Figure 3-3: Static contact angle measurements for DI water on (a) natively oxidized and (b) nanoporous AAO aluminum surfaces.

3.1.2 Pool Boiling Performance

Using the aforementioned pool boiling setup, a subcooled pool boiling study was conducted on both natively oxidized and AAO aluminum samples. To study the effects of surface orientation on boiling performance, samples were tested in both horizontal and vertical orientations; an example of the horizontal orientation is shown in **Figure 2-1**. The results of experiments conducted in the horizontal orientation are summarized in **Figure 3-4** while the results of experiments conducted in the vertical orientation are summarized in **Figure 3-5**. Sample performance was evaluated by the attained heat flux for a given surface superheat where heat flux was obtained by dividing the heater power draw by the known nominal sample surface area. The superheat value ΔT is defined as the temperature difference between the saturation temperature of the fluid and the temperature of the sample as reported by the thermocouples. All pool boiling experiments were conducted at atmospheric pressure where the saturation temperature of NovecTM HFE-7100 was 61 °C.

In both orientations, both the natively oxidized and AAO samples performed nearly identically within the natural convection regime ($\Delta T < 5^\circ\text{C}$); data reported within this regime for both surface finishes fell within the experimental uncertainty of one another. In the horizontal orientation, the heat flux of the natively oxidized surfaces was seen to be

generally greater than that of the AAO surfaces at higher superheat values with the best performing AAO sample overlapping the worst performing natively oxidized sample. In the vertical orientation, both surface finishes demonstrated similar heat fluxes with the exception of AAO Sample 3, which was an outlier in both orientations due to its unusually early onset of CHF. The onset of CHF for AAO Sample 3 in each orientation is denoted by the change in concavity of the plots from concave up to concave down.

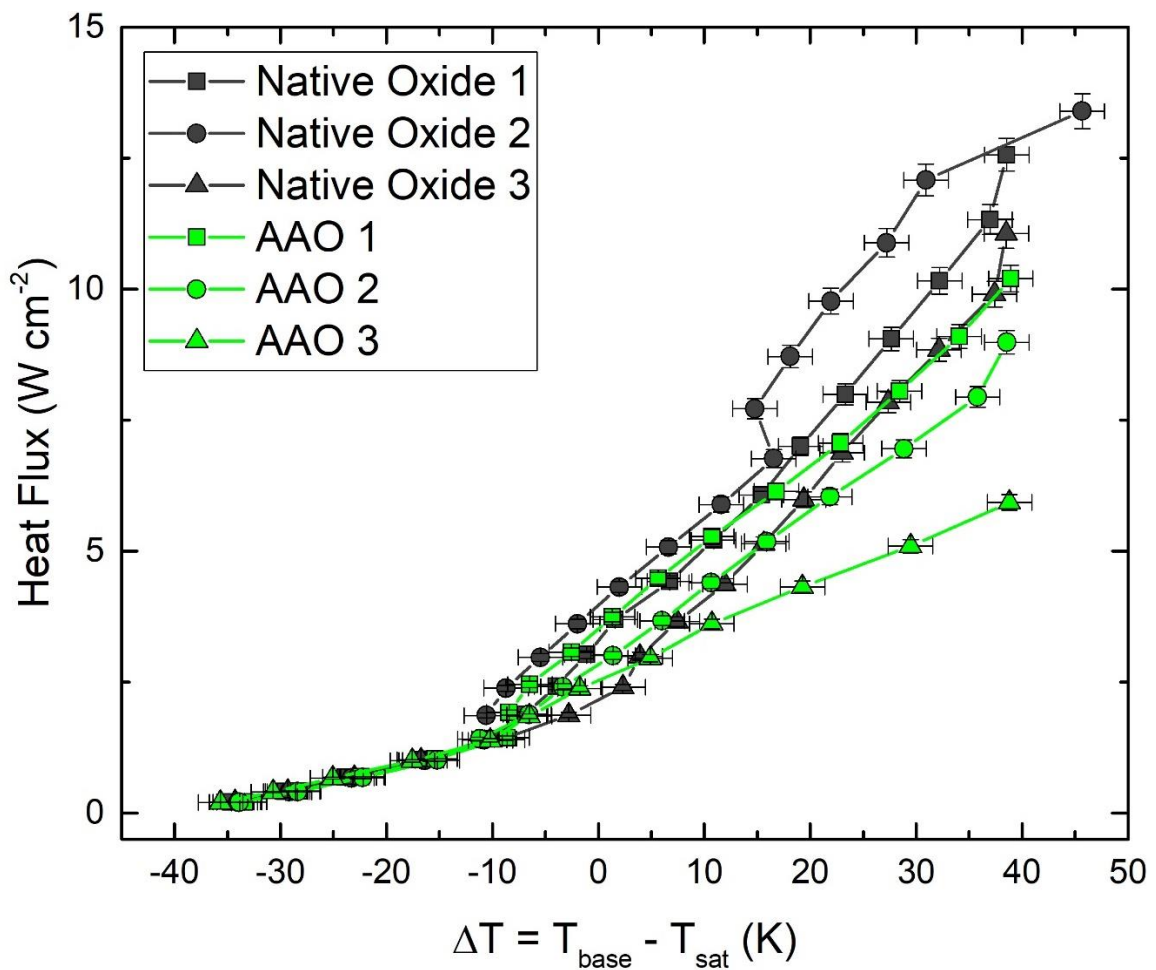


Figure 3-4: Pool boiling performance of natively oxidized and AAO aluminum samples in the horizontal stage orientation.

Examining the effects of orientation on pool boiling performance, native oxide samples demonstrated a 10-15% decrease in heat flux at higher superheats when going

from horizontal to vertical orientation. This discrepancy in heat flux with respect to surface orientation agrees with previous findings for planar surfaces in HFE-7100 [8]. Contrary to natively oxidized samples, AAO samples demonstrated no noticeable orientation dependence. This lack of orientation dependence serves as a contributing factor to the overlap seen in heat flux values for both surface finishes in the vertical orientation.

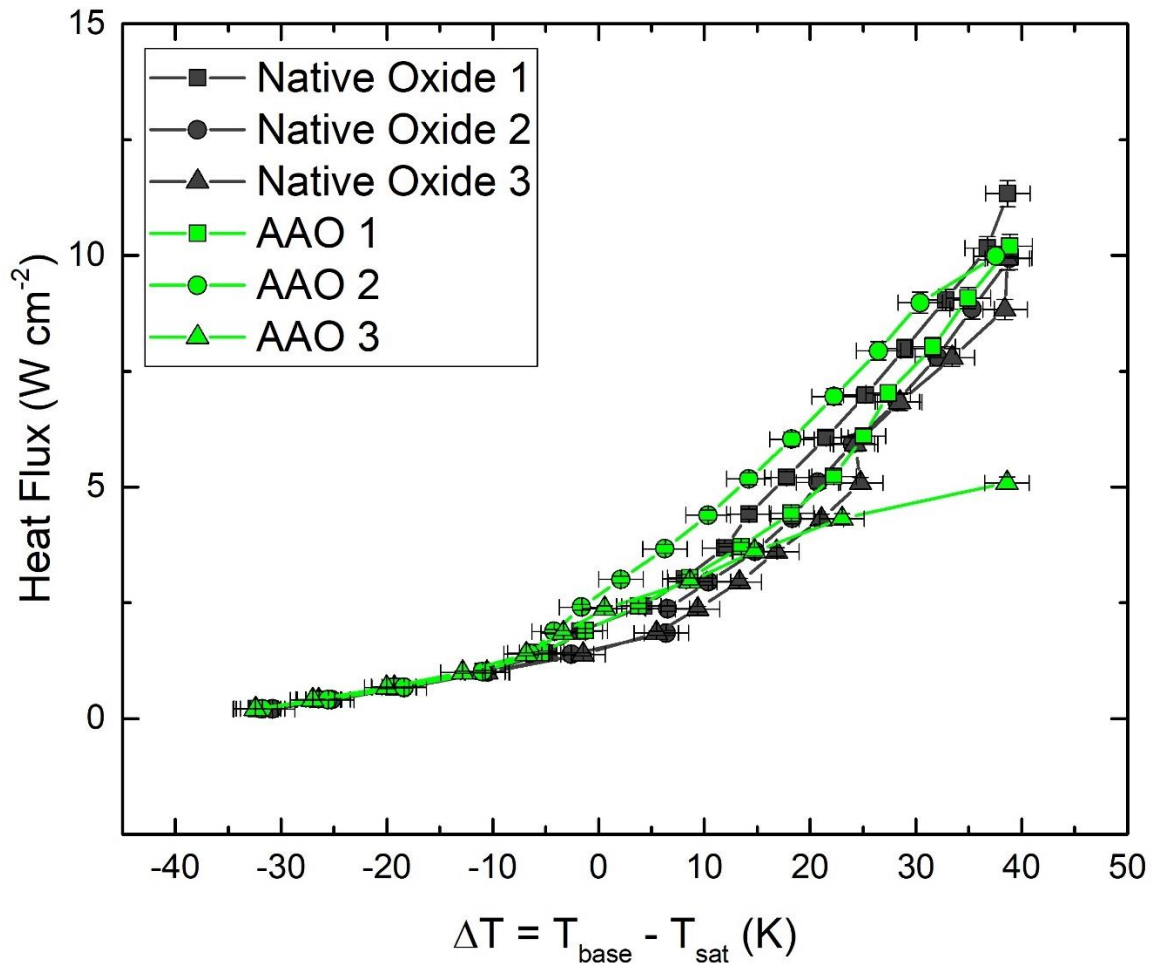


Figure 3-5: Pool boiling performance of natively oxidized and AAO aluminum samples in the vertical stage orientation.

3.1.3 Discussion of Results

Based on the above results, there appear to be no boiling heat transfer improvements observed by nanoporous AAO coatings over natively oxidized aluminum

surfaces despite the improved wettability of AAO surfaces. More closely analyzing this, the first point of interest is the lack of measurable difference in natural convection heat transfer between AAO and natively oxidized surfaces. This seems to be a counterintuitive result as one of the perceived advantages of nanostructured surfaces over their planar counterparts is their enhanced exposed surface area. Thus, the lack of measurable difference in convective heat transfer between the two surface finishes calls into question the ability of AAO nanopores to enhance the wetted surface area of samples. To evaluate this, the wetting model developed by Ran et al. was utilized to determine the ability of the NovecTM HFE-7100 to enter and wet the nanopores present in the AAO layer [21]. In this model, a force balance between the capillary force and the resistive force associated with air trapped in a nanopore upon initial wetting is used to determine the penetration depth of water into the nanopore. A schematic representation of this interaction is shown in the inset of **Figure 3-6(b)**. The model predicts penetration depth h as

$$h = \frac{4L\gamma\cos(\theta)}{P_0d + 4\gamma\cos(\theta)} \quad \text{Eq. 3-1}$$

where L is the pore depth (14 μm), γ is the surface tension of the fluid (13.6 mN m^{-1} for NovecTM HFE-7100, 72 mN m^{-1} for water), θ is the static contact angle of the native oxide (5 degrees for NovecTM HFE-7100, 81.1 degrees for water), P_0 is the initial gas pressure of the trapped air (1 atm), and d is the pore diameter (80 nm). Defining sidewall wetting as $\frac{h}{L}$ and plotting the results of the Ran model in terms of sidewall wetting as a function of surface tension and pore diameter for both water and NovecTM HFE-7100, the plots shown in **Figure 3-6** were generated. Using the γ value for NovecTM HFE-7100 and an average pore diameter of 80 nm, a predicted sidewall wetting value $\frac{h}{L}$ of 87 % was obtained, as

shown in **Figure 3-6(a)**. Using this sidewall wetting value, the improvement in wetted surface area due to the presence of nanopores could be calculated by assuming the nanopores to be cylindrical in shape and calculating the surface area improvement of a single nanopore. Once the surface area improvement of a single nanopore was found, this value was scaled by the nanopore density to obtain the overall surface area improvement factor. Details of the surface area enhancement calculations made for AAO surfaces can be found in **Appendix D**. Based on the obtained value for sidewall wetting and the pore geometry shown in **Figure 3-2**, AAO samples were estimated to possess a $\sim 400x$ greater wetted surface area than natively oxidized samples, confirming the notion that AAO nanopores improve the wetted surface area of samples while simultaneously raising questions as to what could be contributing to the diminished boiling heat transfer performance observed for AAO samples.

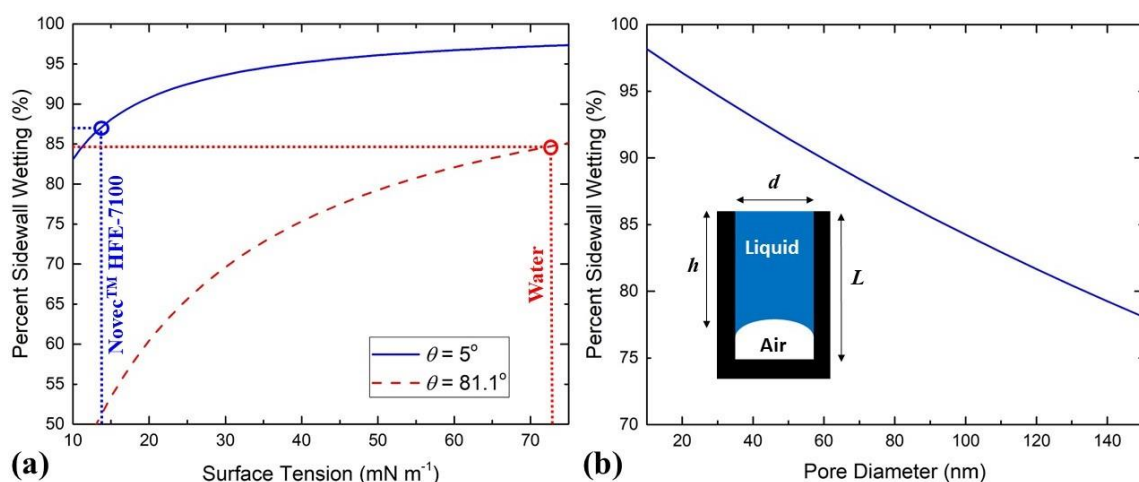


Figure 3-6: Percent sidewall wetting as a function of (a) surface tension for both water and Novec™ HFE-7100 and (b) pore diameter. The inset of (b) schematically demonstrates the force balance described by the Ran model.

While nanoporous AAO surfaces have been shown to possess far greater wetted surface area than their natively oxidized counterparts, there are other factors introduced by the presence of an epitaxial AAO layer that could negatively impact the boiling heat transfer performance of samples that should be accounted for. One possible factor is the increased thermal resistance of the thicker AAO layer compared to the native oxide layer. While the natively oxidized layer thickness is on the order of ~10 nm, the average thickness of the AAO layer is ~14 μm . By adopting a simple 1-D planar wall conduction model

$$R_{th,AAO} = \frac{\Delta T_{AAO}}{Q} = \frac{t}{\kappa A} \quad \text{Eq. 3-2}$$

where ΔT_{AAO} is the temperature difference between the AAO surface and AAO/Al interface, Q is the total heat flow through the sample perpendicular to the film of area A , t is the thickness of the AAO layer, and κ is the effective thermal conductivity of the AAO layer filled with NovecTM HFE-7100, the impact of the difference in layer thickness can be evaluated. Using a κ value of .53 $\text{W m}^{-1} \text{K}^{-1}$ for the AAO layer [35] and an average oxide thickness of 14 μm , the thermal resistance of the AAO layer was found to be 0.14 K W^{-1} . Multiplying this thermal resistance by each heat flux value and subtracting the result from the measured superheat, a closer approximation of the actual surface superheat at the AAO/fluid interface was obtained. After adjusting **Figure 3-4** to accommodate the new surface superheat approximations, the resulting plot shown in **Figure 3-7** now shows comparable performance between AAO and native oxide samples within experimental error. This finding suggests that the AAO film imposes a small degradation in boiling performance due to the AAO layer thickness while not noticeably improving boiling performance by enhancing wetted surface area.

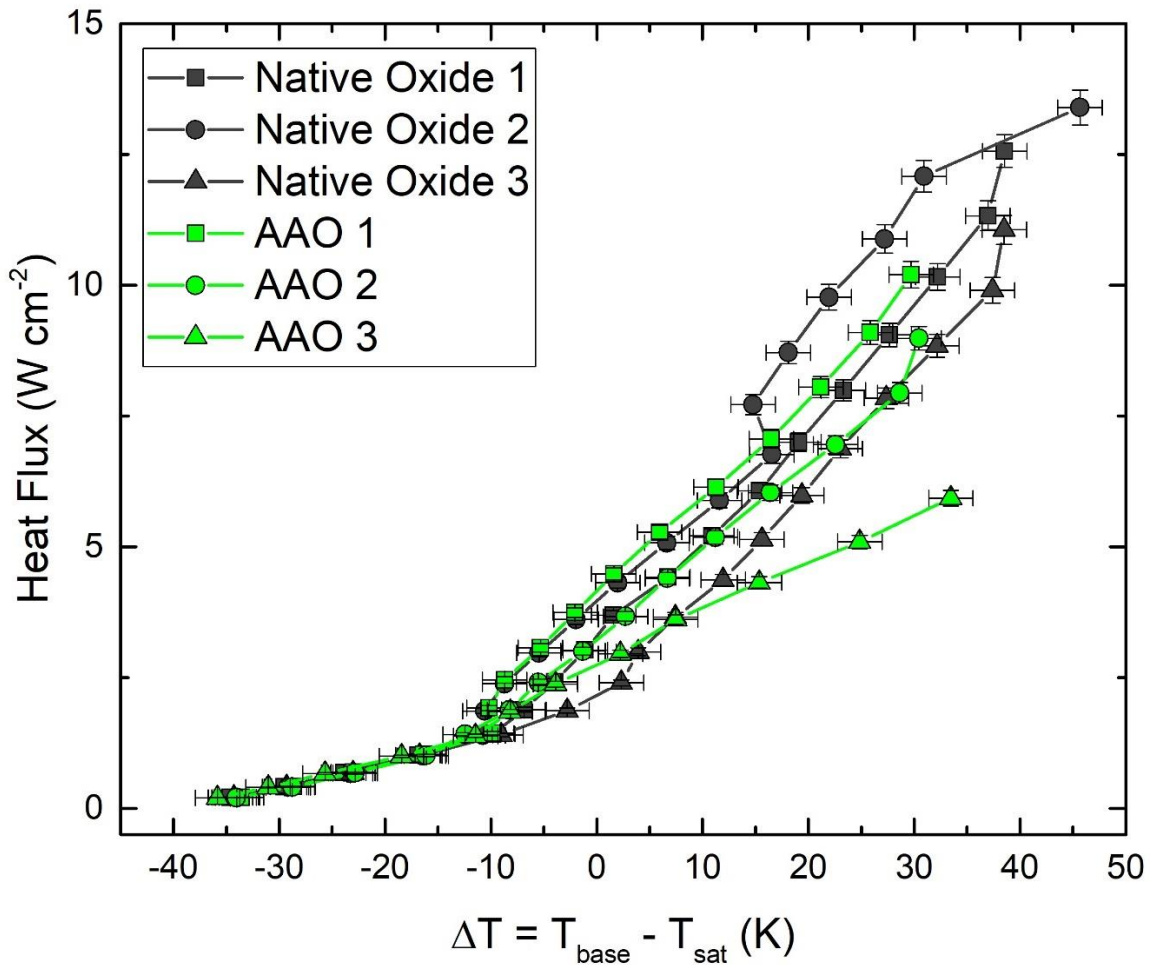


Figure 3-7: Adjusted pool boiling performance for samples in the horizontal stage orientation. Superheat values for AAO data points have been shifted down by the AAO/fluid thermal resistance-heat flux product.

To examine the effects of the AAO layer on nucleation site density, still images captured during boiling experiments were reviewed. Shown in **Figure 3-8**, native oxide samples were observed to have higher nucleation site densities than AAO samples at the onset of nucleate boiling. This discrepancy contradicts the expectation that an increased number of nanopores would lead to an increase in nucleation site density. Instead, it is possible that the small scale of the surface features present on the nanoporous AAO layer lowers the roughness of the sample surface, reducing the ability of the surface to develop

nucleation sites. While studying the effects of AAO films on boiling heat transfer, Kim et al. proposed that boiling enhancements in water could be due to larger surface features such as microscale pits, voids, or defects instead of the nanopores themselves[36]. In the present work, it is believed that due to the low surface roughness resulting from the high quality of surface finish on the AAO samples, the ability of the surfaces to facilitate nucleation sites was negatively impacted.

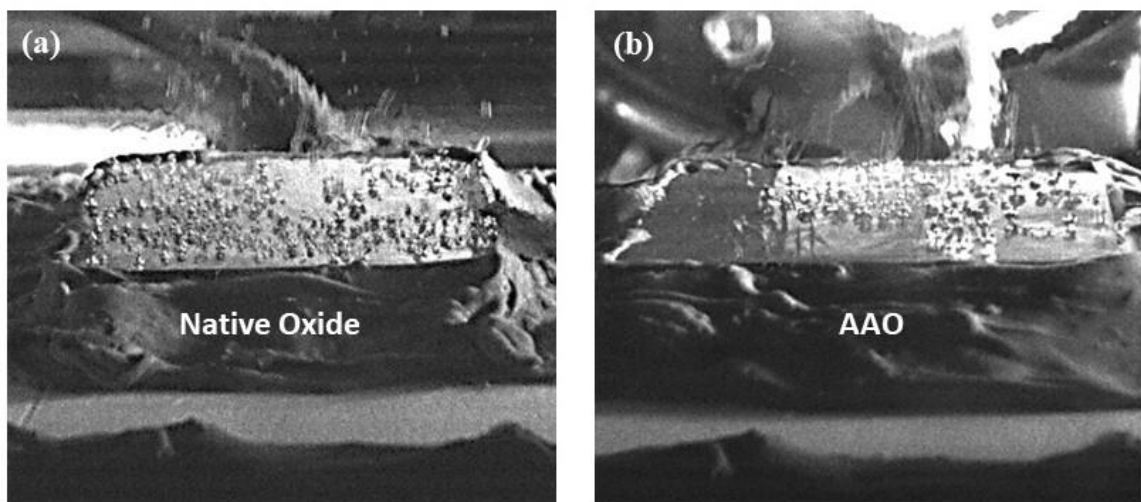


Figure 3-8: Still images taken at the onset of nucleate boiling ($\Delta T = \sim 0-5$ K) for (a) native oxide and (b) AAO samples in the horizontal orientation.

To further examine the effects of the nanoporous AAO layer on nucleation, the analytical model originally developed by Hsu to predict the size range of effective nucleation cavities in water, pentane, and ether was employed[37]. Based on the thermophysical properties of a fluid, Hsu predicted the size range of active nucleation sites on a surface as a function of superheat, pool subcooling, and contact angle. Using this model with the thermophysical properties of NovecTM HFE-7100 and the subcooling conditions present in this work, the size range of active nucleation sites was found and is shown in **Figure 3-9**. As can be seen in **Figure 3-9**, the size range of active nucleation sites

predicted by the Hsu model is on the order of 0.1-800 μm whereas the nanopore radii for samples studied in this work fall outside of the range for active nucleation site at 20-70 nm. This finding further suggests that the nanopores present on AAO samples do not contribute to nucleation site density and that microscale surface defects, if present, would likely improve the nucleate boiling performance of the AAO samples.

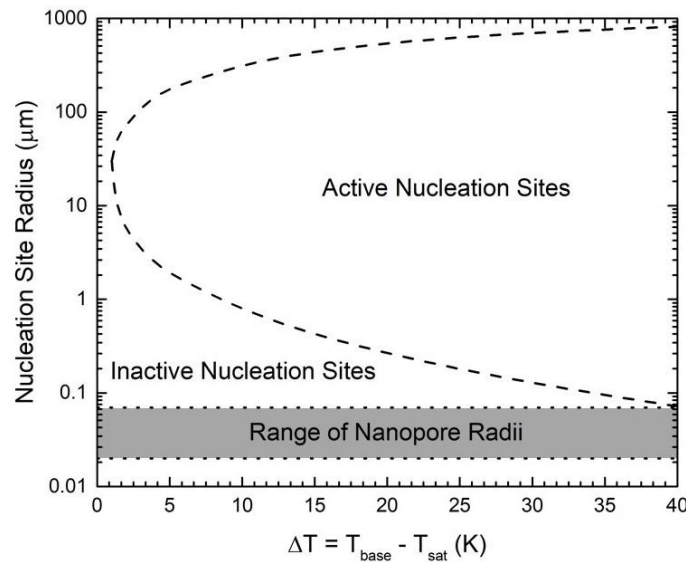


Figure 3-9: Size range of active nucleation sites predicted by the Hsu model for Novec™ HFE-7100 compared to the size range of nanopore radii for samples studied in this work.

Looking at the use of nanoporous AAO surfaces as an inverse analogue to nanowire arrays, the findings of this study suggest that AAO coatings neither increase nucleation site density nor enhance the wetting behavior of samples. While AAO surfaces do show greatly improved wetted surface areas, the results obtained from pool boiling studies in this work suggest that improved wetted surface area offered by the nanoscale features of the AAO layer does not significantly enhance the pool boiling performance of the AAO samples.

3.2 Copper Oxide Nanostructure Surfaces

To contrast with nanoporous AAO surfaces, the boiling heat transfer effectiveness of copper oxide (CuO) nanostructure surfaces was also investigated. The CuO nanostructure coatings studied in this work were synthesized using a two-cycle rapid oxidation process. Prior to oxidation, C101 copper squares were first sanded to strip away the pre-existing native CuO layer. Following sanding, samples were placed in an ultrasonic bath and blown dry with nitrogen to remove surface contaminants and residual surface particles from sanding. Immediately before oxidizing, samples were dipped in a 3 M hydrochloric acid (HCl) solution for 30 seconds, rinsed with DI water, and blown dry with nitrogen to remove any recently formed surface oxide. Directly after drying, samples were placed into a bath of dilute ammonia hydroxide heated to 60 °C for nanostructure synthesis. Two 4-hour oxidizing cycles were performed on samples; between cycles, samples were rinsed with DI water, blown dry with nitrogen, and a new oxidizing solution was prepared for the following cycle. An image of the resulting nanostructure-coated surface is shown in **Figure 3-10(c)**.

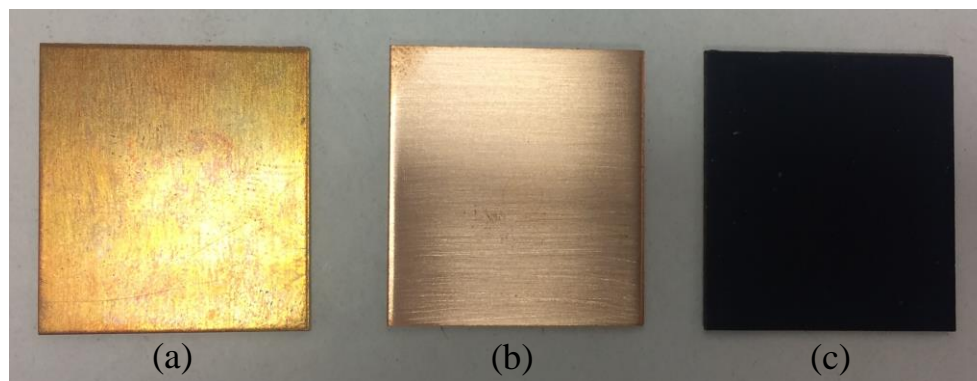


Figure 3-10: Left to right: (a) as-received copper square with native oxide, (b) sample after sanding and HCl dip, (c) nanostructure-coated sample after second oxidation cycle.

3.2.1 Surface Characterization

Following synthesis, samples were inspected using an Amray 1830 SEM/energy dispersive spectrometry (EDS) system. SEM imaging was used to measure the length of nanostructures on the surface of the sample while EDS was used to verify the elemental composition of the CuO nanostructure coating. From SEM images, like the one shown in **Figure 3-11**, the average nanostructure length was found to vary between 1 μm and 2 μm with an average value of approximately 1.6 μm .

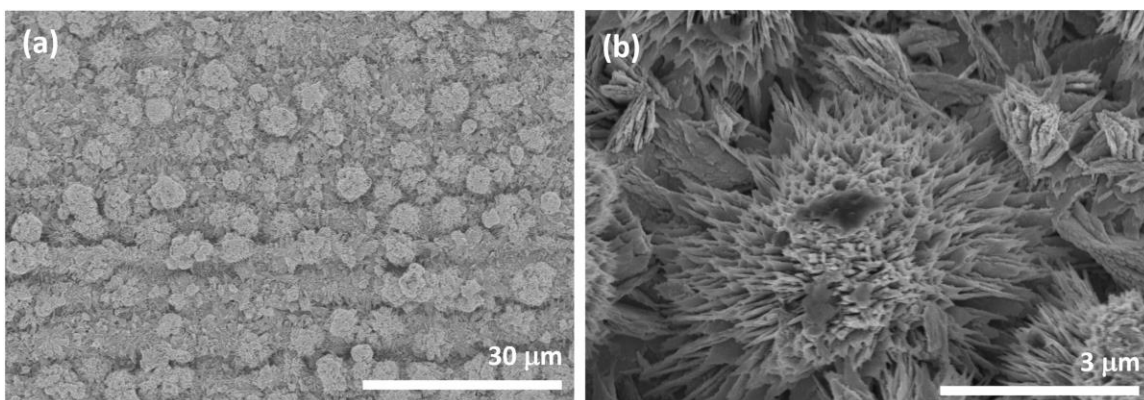


Figure 3-11: SEM images depicting CuO nanostructures. Image (a) shows multiple nanostructures while (b) shows an individual nanostructure.

From the EDS spectrometry shown in **Figure 3-12**, surface elemental content for the CuO nanostructure samples was verified to be predominantly copper and oxygen with some minor silicon contamination introduced by sanding. The dominant presence of Cu in relation to O may also be due to signal from the underlying Cu substrate.

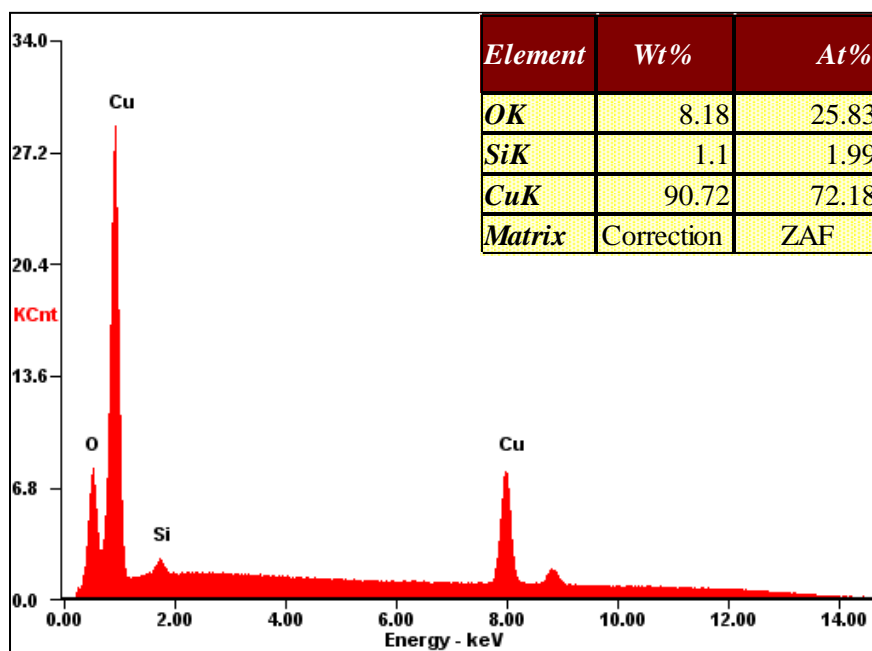


Figure 3-12: EDS scan of CuO nanostructure coated sample surface.

Similar to the AAO and natively oxidized aluminum samples, the wetting behavior of the natively oxidized and CuO nanostructure coated surfaces was characterized by measure of static contact angle, as shown in **Figure 3-13**. Attempts at measuring the static contact angle using NovecTM HFE-7100 resulted in too low of contact angles to accurately measure so DI water was instead used to measure the static contact angle for each surface. For natively oxidized samples, the average static contact angle value was found to be 108.0 degrees, implying a low degree of surface wettability. Meanwhile, for CuO nanostructure coated samples, the average static contact angle was measured to be 124.4 degrees, suggesting that CuO nanostructure coatings further increase the hydrophobicity of copper surfaces.

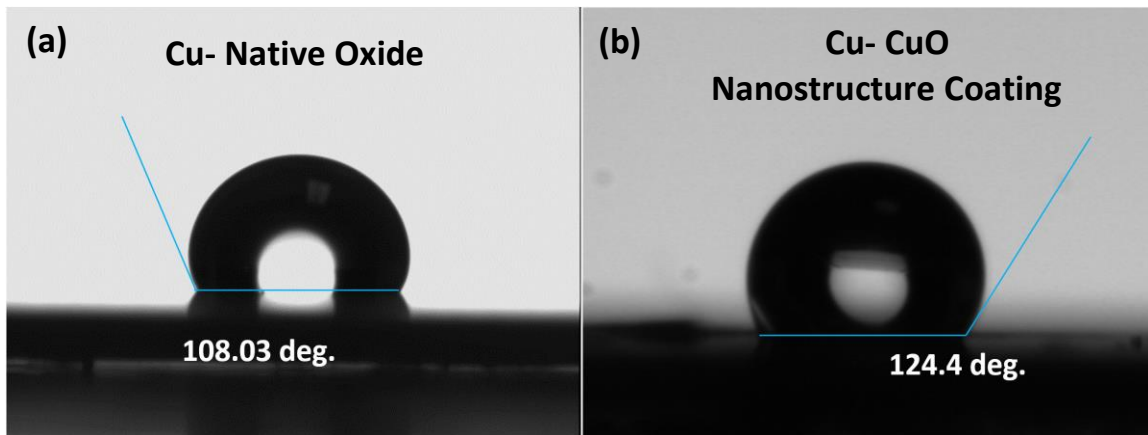


Figure 3-13: Static contact angle measurement for DI water on (a) natively oxidized and (b) CuO nanostructure coated copper surfaces.

3.2.2 Pool Boiling Performance

To observe the boiling heat transfer effectiveness of CuO nanostructure coatings on copper surfaces, a subcooled pool boiling study was conducted on natively oxidized and CuO nanostructure coated copper surfaces using the above pool boiling setup. In this study, both natively oxidized and CuO nanostructure coated copper surfaces were evaluated in only the horizontal orientation where sample performance was based on the maximum boiling heat flux achieved by each sample. The results of this study are summarized in **Figure 3-14**. As with the native oxide/AAO aluminum study, all experiments were conducted at atmospheric pressure and the superheat value is defined as the temperature difference between the saturation temperature working fluid and the reported temperature of the sample.

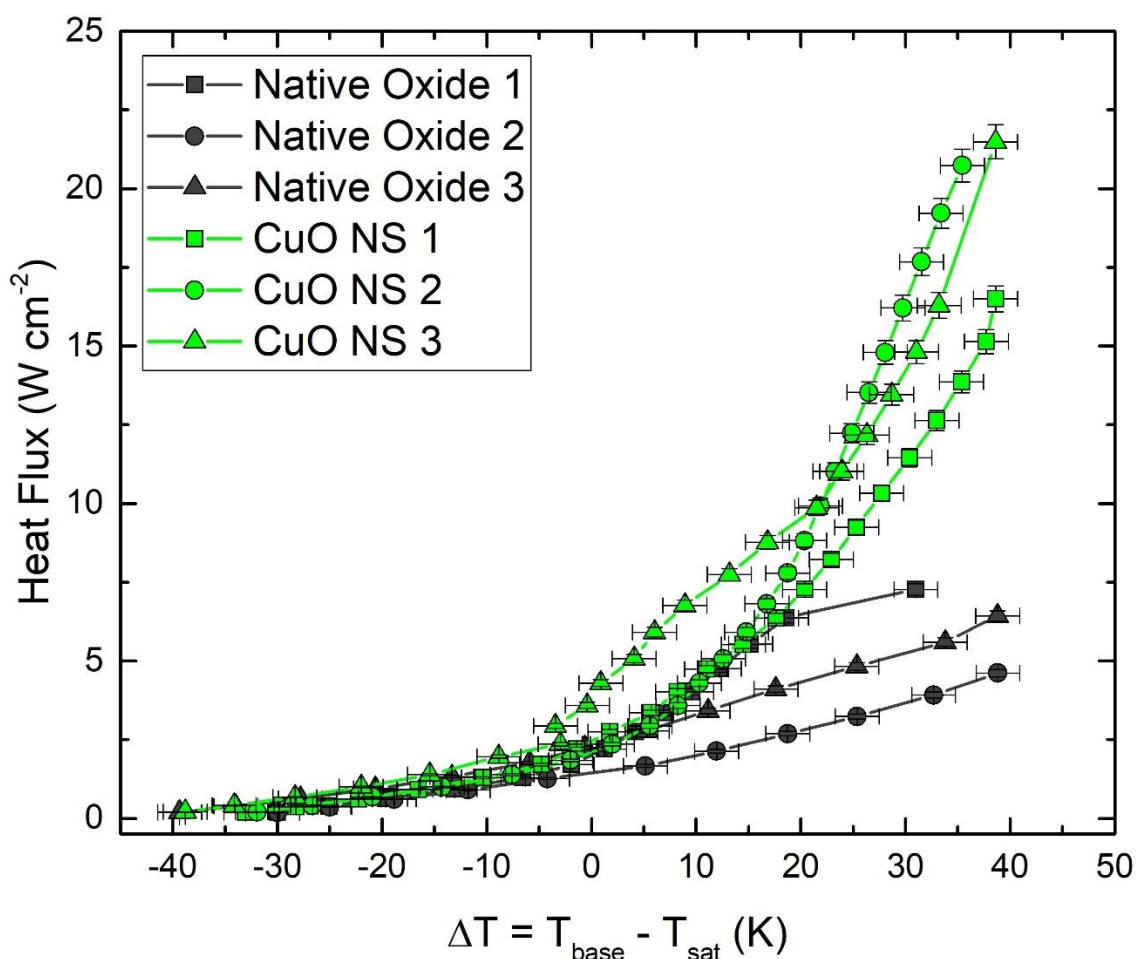


Figure 3-14: Pool boiling performance of natively oxidized and CuO nanostructure coated copper samples.

In all cases, the CuO nanostructure coated surfaces greatly outperformed their natively oxidized copper counterparts. Typical peak heat flux values for natively oxidized copper samples ranged from 4 W cm^{-2} to 7.5 W cm^{-2} while typical peak heat flux values for CuO nanostructure coated samples ranged from 16.5 W cm^{-2} to 21.5 W cm^{-2} , showing a greater than two-fold improvement in heat flux for CuO nanostructure coated samples over natively oxidized copper samples. Additionally, still images shown in **Figure 3-15** show greatly enhanced nucleation activity on CuO nanostructure coated surfaces over natively oxidized copper surfaces at similar superheat. Based on the observations made in

this study, it is believed that CuO nanostructure coatings can offer improvements in boiling heat transfer performance at lower heat fluxes through increased hydrophobicity, as shown in **Figure 3-13**, and increased nucleation activity, as shown in **Figure 3-15**.

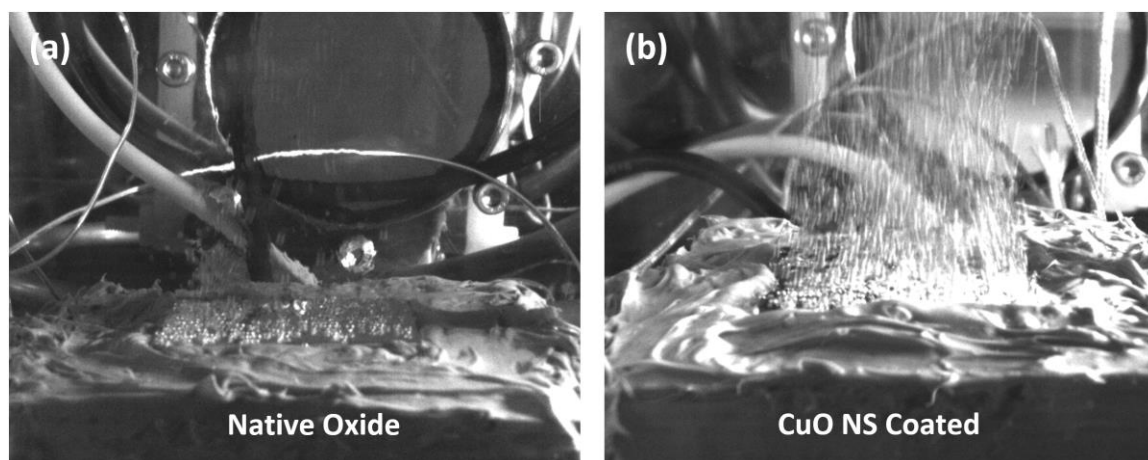


Figure 3-15: Still images taken at 40 K of superheat for (a) native oxide and (b) CuO nanostructure coated samples in the horizontal orientation.

3.2.3 Conclusions

The influence of porous and protrusive nanostructure coatings on pool boiling heat transfer performance was investigated. For nanoporous AAO coated samples, slightly diminished pool boiling heat transfer performance compared to natively oxidized samples was observed despite large improvements in the wetted area of AAO samples over natively oxidized samples. As of result of the AAO pool boiling study, increased surface area as a contributing factor to pool boiling heat transfer enhancement was isolated for independent examination. The results of the present AAO study show increased surface area to play a minimal role in improving the boiling heat transfer performance of nanostructure coated samples in isolation, suggesting that enhancing wettability and nucleation activity may instead be more effective strategies for improving boiling heat transfer performance. For protrusive CuO nanostructure coated samples, increased hydrophobicity and greatly

enhanced boiling heat transfer performance were observed compared to natively oxidized samples. This leads to the belief that increasing hydrophobicity and nucleation site density can be an effective strategy for enhancing the boiling heat transfer performance of a given surface through nanostructure surface enhancements. However, further study on the isolated effects of each of these strategies is desired so that the individual contributions of each strategy towards improving the boiling heat transfer performance of a surface through nanoscale enhancements may be fully understood.

CHAPTER 4

HIGH-THROUGHPUT 1D ROLL-MOLDED MICROFIN ARRAY SURFACES

An important feature of any practical surface enhancement technology is the ability to scale production of that technology to meet industrial demand. While many surface technologies developed in literature offer significant improvements to boiling heat transfer, the economic scalability of these technologies is yet to be demonstrated[13,20,33]. One such surface enhancement technology that would be realizable at an industrial scale is the use of roll-molding to produce 1D microfin array surfaces. Due to this capability, the pool boiling performance of high-throughput roll-molded 1D microfin array surfaces was investigated. The microfin samples studied in this work were obtained through a collaboration with the Wen Jin Meng group from LSU. Microfin samples were fabricated through a roll-molding process using three different compression forces to vary channel width and fin height[31]. During the roll-molding process, samples were plastically deformed by a constant pitch roller sleeve to form 1D microfin arrays. Fins formed by this roll-molding process were oriented in the same direction as the direction of rolling. The three compression forces used to form microfin arrays were 5000 lbf, 15000 lbf, and 23000 lbf. The resulting microfin geometry for each compression force is shown in **Figure 4-1**.

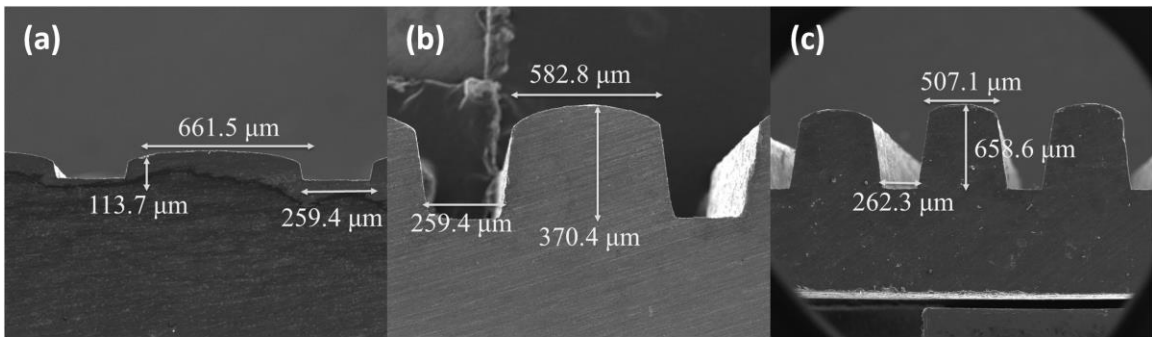


Figure 4-1: Cross-sectional images depicting fin geometry for microfin arrays generated using compression forces of (a) 5000 lbf, (b) 15000 lbf, and (c) 23000 lbf.

4.1 Preliminary Surface Evaluation

4.1.1 Pool Boiling Performance

To evaluate the effectiveness of 1D microfin arrays for immersion cooling applications, a subcooled pool boiling study was performed on samples fabricated using each of the three roll molding forces. Planar, unmodified aluminum samples were also included in the study to serve as a control group for comparing the performance of roll-molded samples to. Samples were tested in both horizontal and vertical stage orientations. In the vertical stage orientation, microfin samples were mounted such that the fins were vertically oriented. The results of experiments conducted in the horizontal stage orientation are summarized in **Figure 4-2** and the results of experiments conducted in the vertical stage orientation are summarized in **Figure 4-3**.

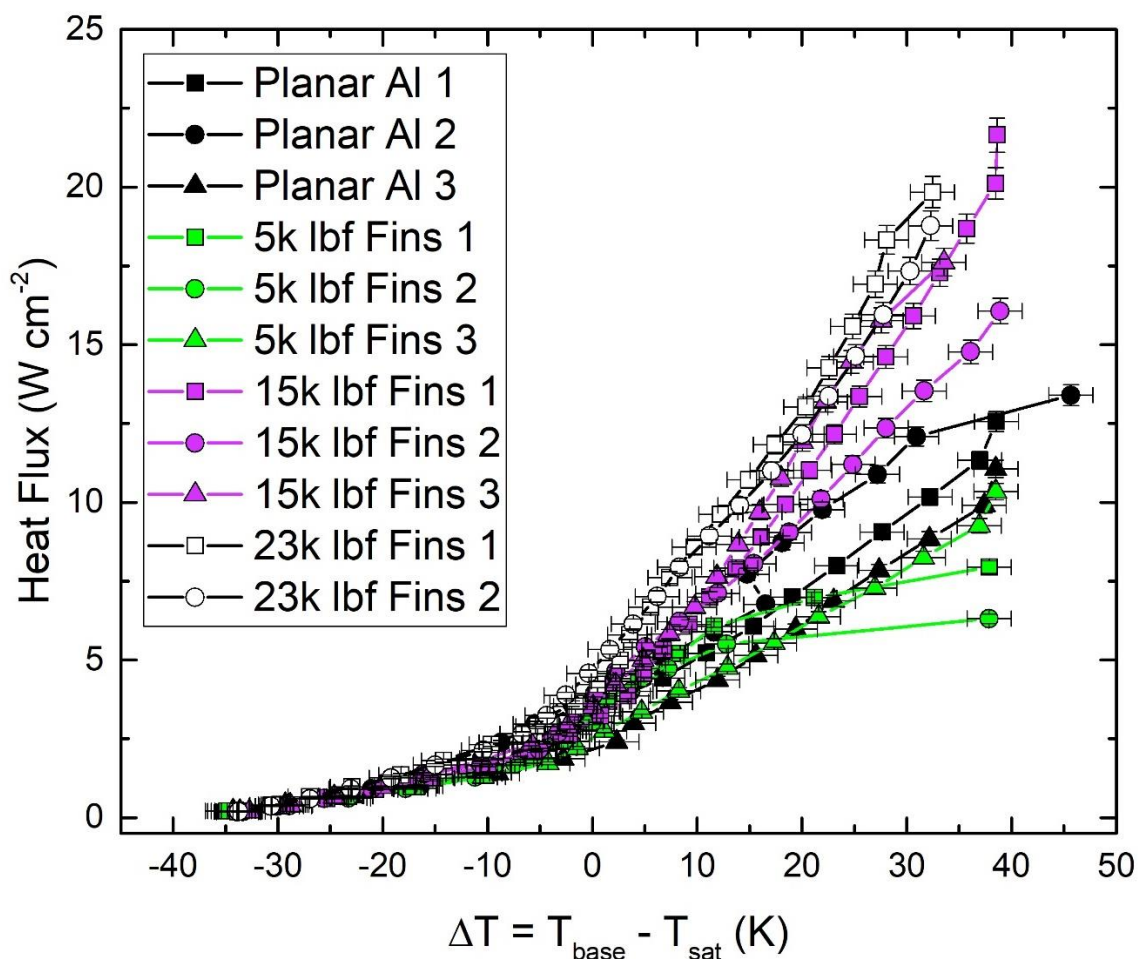


Figure 4-2: Pool boiling performance of 1D roll-molded microfin array samples and planar control samples in the horizontal stage orientation.

In both orientations, microfin samples fabricated using a 23000 lbf roll-molding force generally outperformed samples fabricated using 15000 lbf and 5000 lbf roll-molding forces and planar aluminum controls in terms of heat flux per superheat ΔT . Compared to control samples, 23000 lbf roll-molded microfin samples showed a two-fold improvement in surface heat flux within the nucleate boiling regime ($\Delta T > 5$ K). By contrast, samples fabricated using a 5000 lbf roll-molding force showed the poorest pool boiling performance, with the best performing 5000 lbf sample overlapping the worst planar control sample.

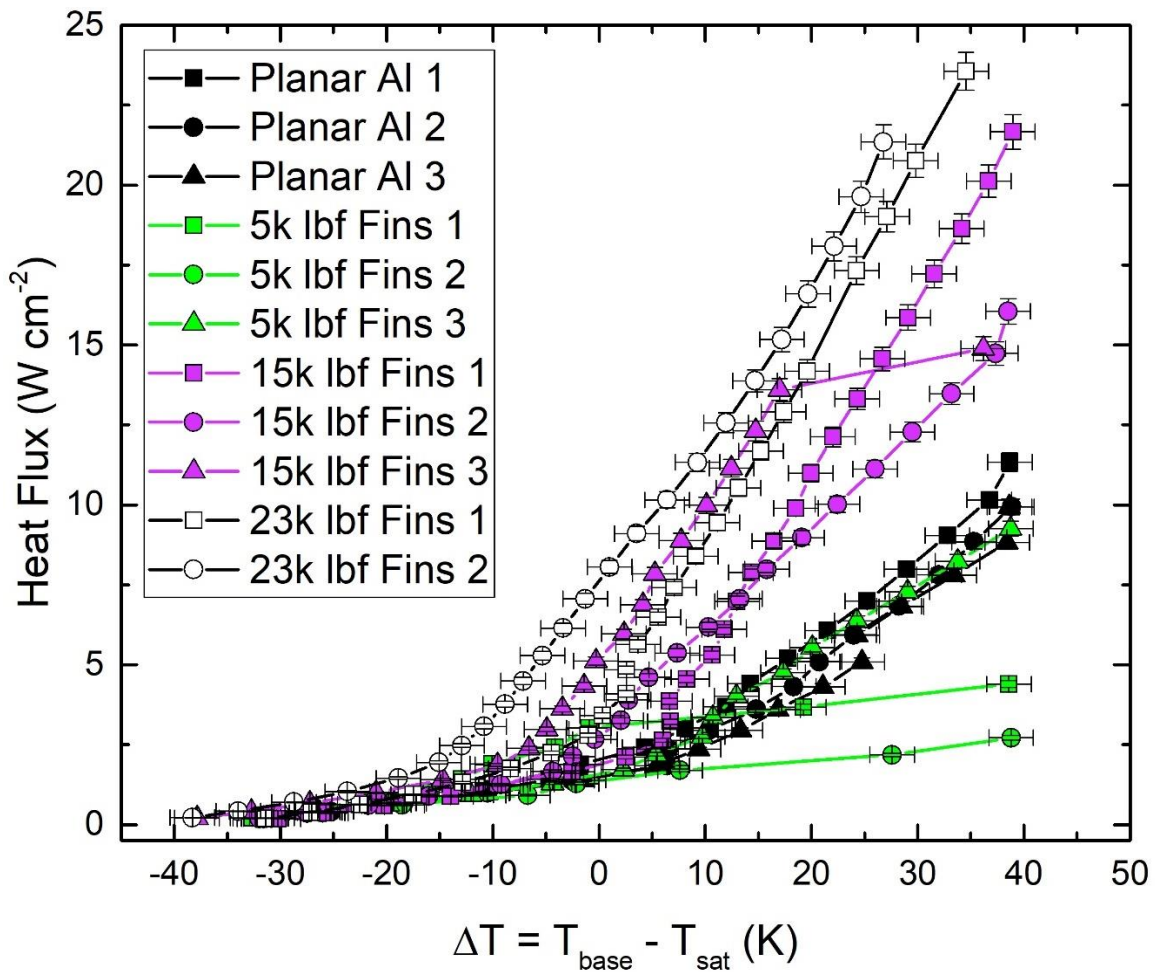


Figure 4-3: Pool boiling performance of 1D roll-molded microfin array samples and planar control samples in the vertical stage orientation.

Examining the effects of orientation on pool boiling performance, samples fabricated using a 15000 lbf roll-molding force showed no discernable orientation dependence while 5000 lbf microfin and planar control samples showed a 10-15% decrease in heat flux at 40 K of superheat in the vertical stage orientation as opposed to the horizontal stage orientation. Samples fabricated using a 23000 lbf roll-molding force showed marked improvements (10-15%) in boiling heat transfer performance when tested in the vertical stage orientation versus the horizontal stage orientation.

4.1.2 Discussion of Results

As mentioned in the introduction, surface microstructures such as microfin arrays and microchannels have been previously reported to demonstrate significant enhancement to subcooled pool boiling performance in dielectric fluids. While similar in morphology to previously reported microchannel surfaces, the surfaces investigated in this work differ by their ability to be mass-produced at low-cost through a high-throughput roll-molding method. The results of the above study confirm previous reported findings and offer additional insights on the influence of channel depth on subcooled pool boiling enhancement.

As with AAO coatings, roll-molded microfin arrays offer an increase in wetted surface area over bare planar surfaces with $\sim 1.2x$, $\sim 1.8x$, and $\sim 2.2x$ more wetted surface area than bare planar samples for 5000 lbf, 15000 lbf, and 23000 lbf samples, respectively. This leads to the expectation that further increasing the wetted surface area of the sample surface would lead to further enhancements in pool boiling performance. However, similarly to AAO coatings, this has been shown not to be the case as past literature shows significantly diminished pool boiling performance for 2D roll-molded microfin array surfaces possessing $\sim 40\%$ greater wetted surface area over their 1D roll molded microfin counterparts [31]. Supporting these observations found in past literature is the performance of the 5000 lbf roll-molded microfin samples. If wetted surface area were the primary factor in enhancing the pool boiling performance for roll-molded microfin array surfaces, then one would expect the 5000 lbf roll-molded samples evaluated in this study to outperform their bare planar counterparts which is not supported by the experimental findings of the present work.

Recalling the work of Cooke et al., a complex relationship between bubble nucleation, migration, and growth has been observed for microchannel surfaces[24]. The previously proposed mechanism of bubble dynamics for microchannel surfaces presented by Cooke et al. suggests that tiny vapor bubbles are initially formed at the base of the channels between microfins. Following formation, the tiny vapor bubbles migrate to the top surface of microfins where they become attached and grow before departure. Since a majority of bubble growth occurs at the top surface of the microfins, the channels between the microfins remain flooded as the size of the initially formed vapor bubbles within the channels is not large enough to lead to dry-out within the channel. By remaining flooded with liquid, the channels act as a liquid supply path for providing subcooled liquid to the top surface of the fins once bubbles have grown and departed. A representative still image captured during a pool boiling experiment and shown in **Figure 4-4** shows large bubbles attached to the top surface of microfins, while much smaller bubbles can be seen migrating from the channels between fins to the top surface of the microfins.

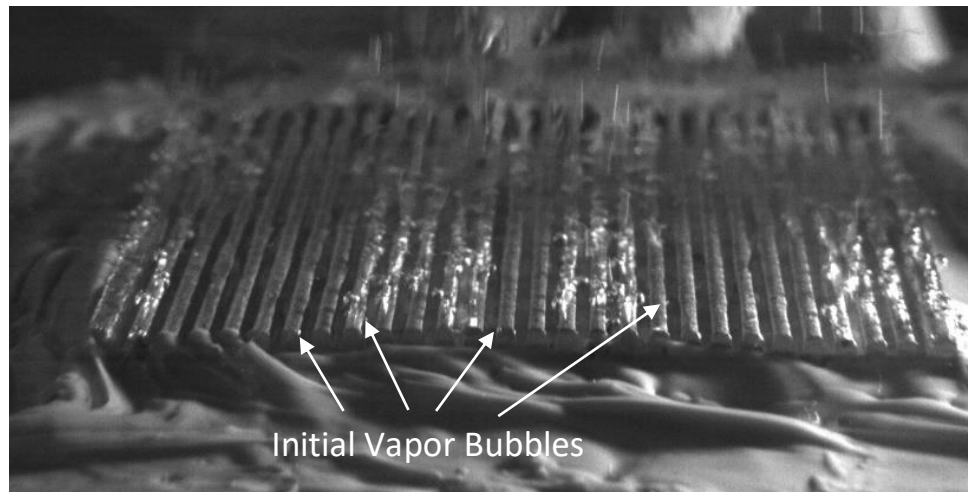


Figure 4-4: Representative still image depicting observed bubble formation behavior. Some of the initially formed vapor bubbles are identified.

Expanding upon the mechanism initially proposed by Cooke, et al., by improving the liquid supply to nucleation sites, rewetting of the heated surface following bubble departure should become more efficient, thus leading to enhancements in subcooled nucleate pool boiling heat transfer. In addition to this, a constant supply of subcooled liquid to nucleation sites would delay the onset of CHF by facilitating the increased liquid demand imposed by the greater nucleation activity associated with higher heat fluxes. **Figure 4-5** shows a representative comparison of nucleation site densities between samples of all roll-molding forces studied in this work. Bare planar control and 5000 lbf roll-molded samples show similar, moderate surface nucleation site densities while 15000 lbf and 23000 lbf roll-molded samples both show much higher nucleation activity, supporting the idea that improved liquid supply can lead to enhancements in subcooled pool boiling performance. As all four stills were taken at similar superheats, this suggests that 5000 lbf roll-molded microfins do not offer any meaningful improvements to subcooled liquid supply for nucleation sites. Additionally, this finding implies that there is a critical channel dimension that exists between the dimensions of the 5000 lbf and 15000 lbf roll-molded microfin channels that acts as a major influencing factor on the pool boiling performance of a given 1D roll-molded microfin array sample.

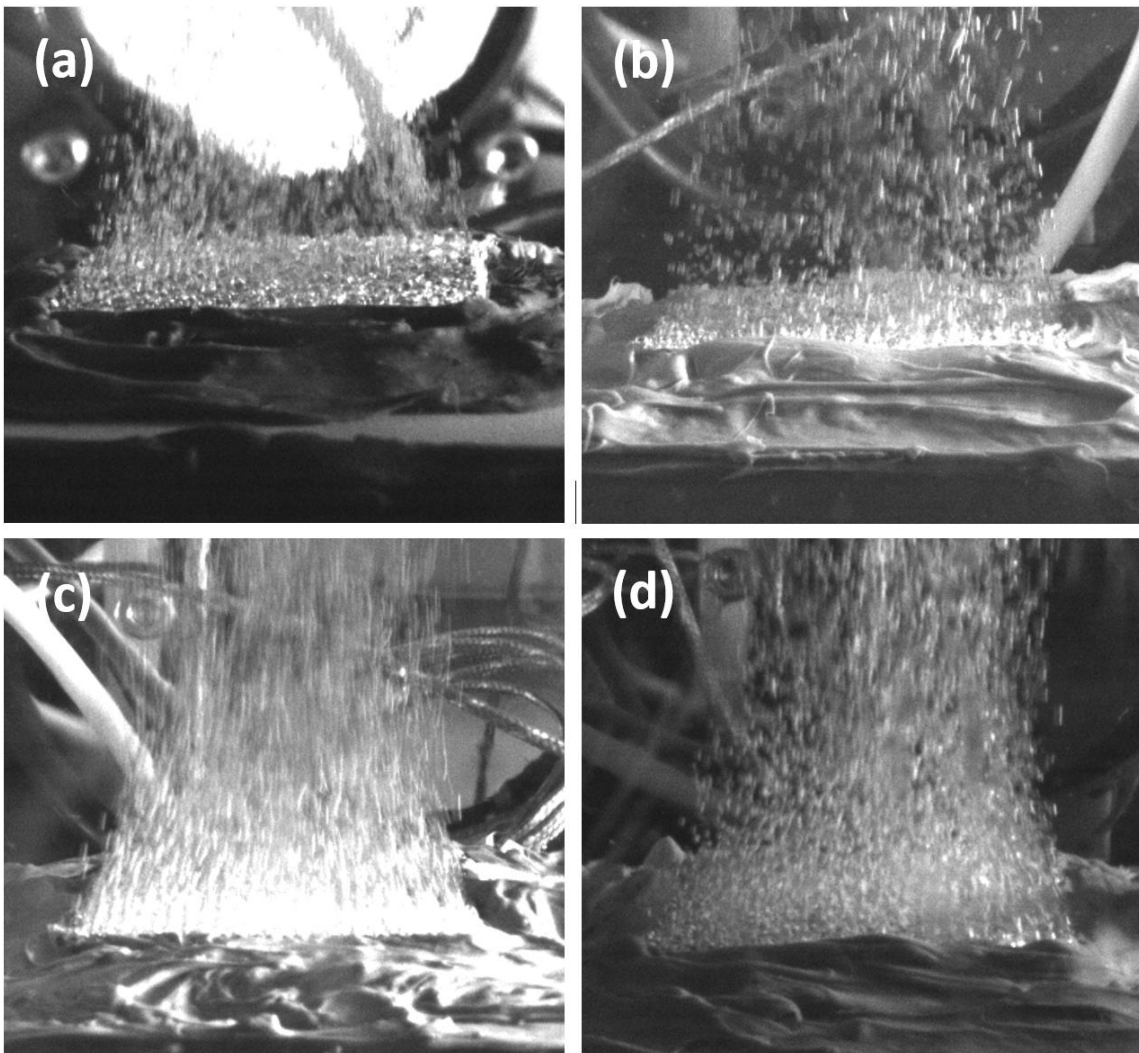


Figure 4-5: Still images taken at $\sim 30\text{-}40\text{K}$ of superheat for (a) planar control, (b) 5000 lbf roll-molded, (c) 15000 lbf roll-molded, and (d) 23000 lbf roll-molded samples.

4.2 Practical Evaluation of Enhanced Surfaces for Immersion Cooling Systems

To quantitatively demonstrate the practical effectiveness of enhanced heat transfer surfaces created through scalable advanced manufacturing techniques within a realistic electronics immersion cooling system, a comparative study was performed on an FPGA with three different cooling configurations: a forced-air cooling system, a liquid immersion system with no attached heat sink, and a liquid immersion system with a 15000 lbf roll-

molded microfin array surface attached. To stress each cooling solution, a Kintex™ 7 FPGA was exercised at increasing power levels for each cooling solution and the steady-state internal temperature of the FPGA was recorded for each power level. Using clock divider circuits as discussed previously, the maximum sustained power draw for the FPGA was measured to be ~16.5W. The results of the comparative study are shown in **Figure 4-6**. The performance of each cooling solution was evaluated based on the steady state excess temperature ΔT achieved for each power level, where ΔT is defined as the difference between the FPGA internal temperature and the ambient fluid (air or Novec™ HFE-7100) temperature. A single K-type thermocouple was used to continuously monitor and record the ambient fluid temperature throughout all experimental trials.

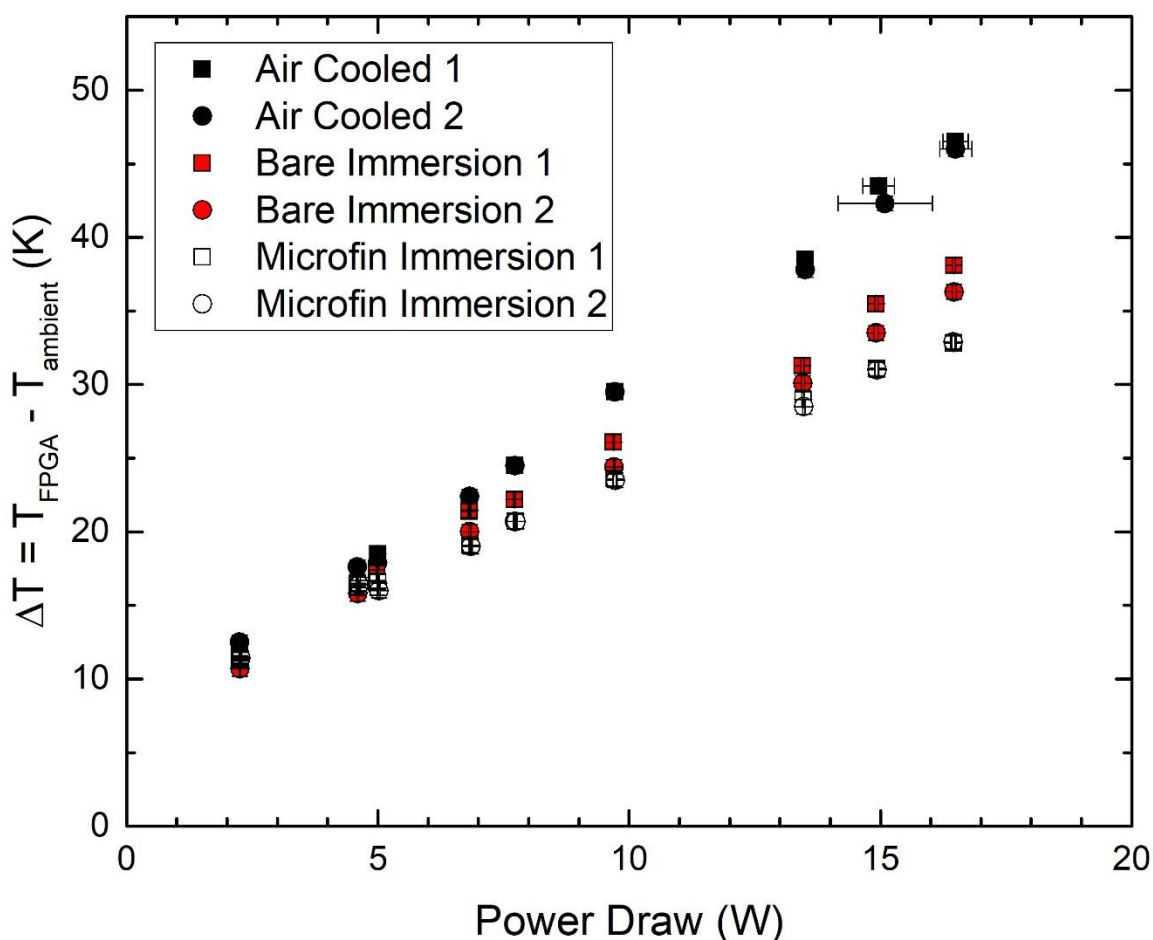


Figure 4-6: Performance summary of cooling solutions for managing the thermal loads produced by the FPGA.

At low power draws (1 W to 5 W), all evaluated cooling solutions managed to produce relatively similar results with the measured steady state ΔT of each cooling solution falling within ± 2 °C of the others. However, past ~7 W of power draw, the steady state excess temperatures achieved by each cooling solution began to stratify. At the highest power draw of ~16.5 W, the excess temperature achieved by the forced-air cooling solution was measured to be ~46.5 °C while the excess temperatures achieved by the bare and microfin surface-mounted immersion configurations were measured to be ~37 °C and ~33 °C, respectively. Taking the slope of each data set, the resulting junction-to-ambient

thermal resistances for each cooling solution were found to be $\sim 2.5 \text{ K W}^{-1}$, 1.8 K W^{-1} , and 1.5 K W^{-1} for the forced-air cooled, bare immersion cooled, and microfin surface-mounted immersion cooled configurations, respectively.

4.2.1 Discussion of Results

Based on the results of this study, the two immersion cooling configurations outperformed the forced-air cooling configuration in managing the thermal loads produced by the FPGA. This was an expected result as the thermal conductivity of NovecTM HFE-7100 ($\sim 70 \text{ mW m}^{-1} \text{ K}^{-1}$) is higher than that of air ($\sim 25\text{-}30 \text{ mW m}^{-1} \text{ K}^{-1}$) for the temperatures encountered in this study. However, among the two immersion cooling solutions, the microfin surface-mounted configuration was found to outperform the bare immersion configuration. This is significant, as for the microfin surface-mounted configuration, there are additional thermal resistances present between the FPGA and the ambient fluid introduced by the FPGA/ microfin surface interface and the added thickness of the attached microfin surface. Additionally, due to the relatively low heat fluxes produced by the FPGA in this study, the nucleate boiling regime was not allowed to fully develop during experimentation, thus limiting the ability of the microfin surface to improve the heat transfer capabilities of the system through enhancements in boiling heat transfer performance. At the $\sim 15 \text{ W}$ and $\sim 16.5 \text{ W}$ power draw levels, the incipience of nucleate boiling was observed for the microfin surface-mounted configuration, while for the bare immersion configuration, only a few errant bubbles were observed to have formed on the bottom surface of the FPGA heat spreader. **Figure 4-7** provides a depiction of the boiling behavior observed for the microfin surface-mounted configuration. The plots resulting from the data for each cooling solution show strongly linear behavior, providing a high

degree of confidence in the reported junction-ambient thermal resistance values for each cooling configuration. The linear behavior of the cooling solutions studied in this work may present the temptation to extrapolate the results of this study out to higher power draws for the FPGA. However, this should be approached with caution as for higher heat fluxes, the relationship between power draw and steady-state excess temperature for the immersion cooling configurations would likely transition to non-linear as the nucleate boiling regime develops.

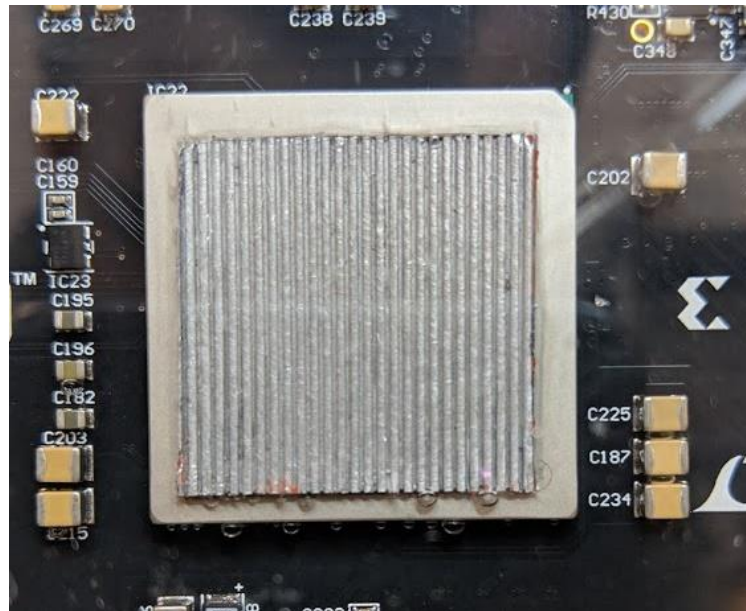


Figure 4-7: Still image taken during immersion cooling testing of the FPGA depicting nucleation on the surface of the roll-molded microfin heat transfer surface.

4.2.2 Conclusions

The ability of high-throughput roll-molded microfin array surfaces to improve pool boiling heat transfer performance was investigated. For samples produced by low roll-molding forces (5000 lbf), a slight reduction in pool boiling heat transfer performance was observed whereas for samples produced by higher roll-molding forces (15000 lbf and

23000 lbf), significant improvements in boiling heat transfer performance were observed. The results of this work suggest that there exists a critical channel dimension between the dimensions of samples produced using 5000 lbf and 15000 lbf of roll-molding force that significantly impacts the pool boiling performance of microfin array surfaces. Using still images captured during pool boiling experiments, the mechanism originally proposed by Cooke et al. that suggests channels between microfins serve as initial vapor bubble formation sites and liquid supply lines to the top surface of microfins was supported. Following the initial investigation of roll-molded microfin array surfaces, a comparative study was performed that evaluated the practical effectiveness of microfin array surfaces in managing the thermal loads produced by a FPGA. In the comparative study, an immersion cooling configuration using a roll-molded microfin array surface mounted to the heat spreader of the FPGA was shown to outperform a conventional forced-air cooling solution and a bare immersion cooling configuration. This result is significant as the production of roll molded microfin arrays is both industrially viable and scalable using current manufacturing technology. To better establish roll-molded microfin array surfaces as an industrially viable technology, further study is required on the influence of surface parameters, such as fin pitch and fin height, on the pool boiling heat transfer performance of microfin array surfaces.

CHAPTER 5

CONCLUSIONS AND FUTURE WORK

5.1 Conclusions

In this work, the ability of micro and nanoscale surface modifications to enhance the pool boiling performance of heat transfer surfaces was investigated. All pool boiling experiments performed in this work utilized a custom pool boiling setup filled with 3M™ Novec™ HFE-7100 dielectric fluid. Experimental trials were automated using a custom LabVIEW™ program to ensure consistent sample-to-sample evaluation. Specific surface enhancement technologies studied in this work include AAO nanopores, CuO nanostructures, and roll-molded microfin arrays. AAO nanopore samples were found to offer no significant improvements to pool boiling behavior over natively oxidized aluminum samples while CuO nanostructure and roll-molded microfin array samples demonstrated significant enhancements in pool boiling behavior over their natively oxidized copper and bare planar aluminum counterparts, respectively. Following the initial investigation of boiling surface performance for each sample type, a comparative study was performed on three different cooling solutions to demonstrate the practical effectiveness of enhanced boiling heat transfer surfaces in an immersion cooling environment. In the comparative study, the cooling performance of a conventional forced-air cooling solution was compared to that of two immersion cooling configurations: one with a custom roll-molded microfin array surface attached to the heat spreader of an FPGA

and one with no attached heat transfer surface. To produce thermal loading, a Kintex 7 FPGA was programmed with a scalable clock divider tree circuit and Microblaze™ soft processor core. The scalable clock divider tree was used to exercise control over the power drawn by the FPGA while the Microblaze™ processor was used to measure and report temperature and power draw information over a UART connection. From the comparative study, the immersion cooling configuration with an attached roll-molded microfin array surface was found to possess the lowest junction-ambient thermal resistance while the forced-air cooling solution had the highest junction-ambient thermal resistance. This demonstration shows the potential impact offered by enhanced boiling surfaces in improving the cooling capabilities of datacenters and HPCs should the technologies studied in this work become accepted by industry.

5.2 Future Work

The AAO samples studied in this work allowed for isolated investigation of the individual impact of enhanced surface area on pool boiling heat transfer performance. To expand upon this, further study focused on the isolated impacts of the other mechanisms used to improve pool boiling heat transfer would be of great interest for future work. When evaluating the pool boiling performance of roll-molded microfin array samples, a significant change in the boiling behavior of samples generated with 5000 lbf and 15000 lbf of roll molding force was observed, leading to the belief that there is a critical channel dimension that strongly affects the boiling heat transfer performance of microfin array samples. Further study on the behavior of samples generated using roll molding forces between 5000 lbf and 15000 lbf to better understand the transition in boiling behavior that occurs between samples generated with these two roll molding forces would be a subject

of interest in future work. Additionally, detailed study of the effects of variations in surface parameters for microfin array surfaces would be of great interest in promoting roll-molded microfin arrays as an industrially viable technology. Expanding upon the improvements offered by CuO nanostructure coated and roll-molded microfin array surfaces, further works focused on the combined effects of the two technologies would be of great interest.

APPENDIX A

IMPORTANT DEFINITIONS AND TERMINOLOGY

Wickability: The ability of a surface to transport fluid through capillary action.

Wettability: Describes the hydrophilicity of a surface. Surface wettability is quantified by static contact angle measurements.

Static Contact Angle: A single drop of liquid (typically water) is dispensed on a surface and the angle made by the liquid/surface interface is measured. Contact angles below 90 degrees indicate objectively hydrophilic behavior while contact angles above 90 degrees indicate hydrophobic behavior. The lower the contact angle, the more hydrophilic a surface is considered to be.

Nucleation Site Density: The number of nucleation sites per unit surface area. Nucleation sites are locations on the heat transfer surface where vapor bubbles consistently form and depart from. In this work, this is qualitatively evaluated based on a visual comparison of samples at similar superheat values.

Nucleation Activity: Qualitative measure of how much nucleate boiling a heat transfer process is generating. Generally speaking, a higher total rate of bubble formation and departure across all nucleation sites corresponds to a greater degree of nucleation activity.

Critical Heat Flux (CHF): The highest heat flux attained by a boiling heat transfer process. On a boiling curve, the onset of CHF is denoted by a change in concavity of the boiling curve from concave up to concave down while the exact value for CHF corresponds to a pronounced peak in heat flux.

Nucleate Boiling Regime: During a heat transfer process, this regime is denoted by consistent formation and departure of bubbles from nucleation sites. This regime begins shortly after the saturation temperature of the working fluid has been exceeded and continues until CHF has been attained.

Film Boiling Regime: This regime is denoted by the formation of a vapor film above the boiling heat transfer surface. Once a boiling process has attained CHF, the heat flux of the heat transfer process decreases with increasing temperature as nucleation sites begin to merge into a continuous vapor film. Between CHF and the fully developed film boiling regime, the heat transfer process is said to be within the transition boiling regime (also called boiling crisis).

Junction-to-Ambient Thermal Resistance: The collective thermal resistance of all elements in a heat transfer process between the silicon die of an integrated circuit and the surrounding ambient fluid. This value is often used to quantify the effectiveness of a thermal management system.

Field-Programmable Gate Array: An integrated circuit that is used to build reconfigurable digital circuits.

APPENDIX B

SCALABLE CLOCK DIVIDER CODE

```
library IEEE;
use IEEE.STD_LOGIC_1164.ALL;
use ieee.std_logic_unsigned.all;
use IEEE.NUMERIC_STD.ALL;

library UNISIM;
use UNISIM.VComponents.all;

entity clock_dividers is
    generic (clk_div_num : integer := 10);
    Port ( R: in STD_LOGIC;
          CLK_IN : in STD_LOGIC;
          clk_div_out : out STD_LOGIC);
end clock_dividers;

architecture rtl of clock_dividers is
    signal tmp: STD_LOGIC_VECTOR(3*clk_div_num downto 1);
    signal clock_out: STD_LOGIC_VECTOR(clk_div_num-1
downto 0);
    signal clock_out_or: STD_LOGIC_VECTOR(clk_div_num-1
downto 1);

begin

    GEN_CLK_DIV: for i in 0 to clk_div_num-1 generate
        process (CLK_IN, clock_out)
            begin
                if CLK_IN'event and CLK_IN='1' then
                    if R='0' or tmp(3*(i+1)) = '1' then
                        tmp((3*(i+1)) downto ((3*i)+1)) <=
(others => '0');
                    else
                        tmp((3*(i+1)) downto ((3*i)+1)) <=
tmp((3*(i+1)) downto ((3*i)+1)) + 1;
                    end if;
                end if;
            end if;
        end process;
    end generate;
end architecture;
```

```

end process;
process (CLK_IN)
begin
    if CLK_IN'event and CLK_IN='1' then
        if R='0' then
            clock_out(i) <= '0';
        elsif tmp(3*(i+1)) = '1' then
            clock_out(i) <= not clock_out(i);
        end if;
    end if;
end process;
end generate GEN_CLK_DIV;

CLK_DIV_OR: for n in 1 to clk_div_num-1 generate
    process(CLK_IN, clock_out, clock_out_or)
    begin
        if n = 1 then
            clock_out_or(n) <= clock_out(0) or
clock_out(1);
        elsif n > 1 and n < clk_div_num-1 then
            clock_out_or(n) <= clock_out(n) or
clock_out_or(n-1);
        elsif n = clk_div_num-1 then
            clock_out_or(n) <= clock_out(n) or
clock_out_or(n-1);
        end if;
    end process;
end generate CLK_DIV_OR;

clk_div_out <= clock_out_or(clk_div_num-1);

end rtl;

```

APPENDIX C

UNCERTAINTY CALCULATIONS

Dimensions of Heat Spreader

$$w := 1 \text{ in} \quad l := 1 \text{ in} \quad t := 4 \text{ mm} \quad A_{base} := w \cdot l = 1 \text{ in}^2 \quad A_{side} := t \cdot w = 0.157 \text{ in}^2$$

Dimensions of PTFE Sample Stage

$$t_{base} := 20 \text{ mm} \quad t_{side} := 12.5 \text{ mm}$$

Dimensions of Power and Thermocouple Leads

$$d_{wire} := 1.5 \text{ mm} \quad d_{TC} := 0.13 \text{ mm} \quad l_{wire} := 12 \text{ in}$$

Thermal Properties

$$\kappa_{PTFE} := 0.25 \cdot \frac{W}{m \cdot K} \quad \kappa_{TCchromel} := 19 \cdot \frac{W}{m \cdot K} \quad \kappa_{TCalumel} := 29.7 \cdot \frac{W}{m \cdot K} \quad \kappa_{wire} := 200 \cdot \frac{W}{m \cdot K}$$

Assuming 40 K Superheat: $\Delta T := 40 \text{ K}$

Calculations: Heat Loss to Surroundings

$$q_{base} := \kappa_{PTFE} \cdot A_{base} \cdot \frac{\Delta T}{t_{base}} = 0.323 \text{ W}$$

$$q_{side} := \kappa_{PTFE} \cdot A_{side} \cdot \frac{\Delta T}{t_{side}} = 0.081 \text{ W}$$

$$q_{wire} := 2 \cdot \kappa_{wire} \cdot \frac{\pi \cdot d_{wire}^2}{4} \cdot \frac{\Delta T}{l_{wire}} = 0.093 \text{ W}$$

$$q_{TC} := 2 \cdot \left(\kappa_{TCchromel} \cdot \frac{\pi \cdot d_{TC}^2}{4} \cdot \frac{\Delta T}{l_{wire}} + \kappa_{TCalumel} \cdot \frac{\pi \cdot d_{TC}^2}{4} \cdot \frac{\Delta T}{l_{wire}} \right) = (1.697 \cdot 10^{-4}) \text{ W}$$

$$q_{total} := q_{base} + 4 \cdot q_{side} + q_{TC} + q_{wire} = 0.741 \text{ W}$$

$$Uncertainty := \frac{q_{total}}{32.85 \text{ W}} = 2.255\%$$

APPENDIX D

AAO SURFACE AREA CALCULATIONS

Sidewall Wetting Value:

$$sww := .87$$

Average Nanopore Dimensions:

$$h := sww \cdot 14 \mu m \quad d_{in_pore} := 80 \text{ nm} \quad d_{out_pore} := 88 \text{ nm}$$

Linear Density of Nanopores:

$$\rho_{pores} := \frac{1}{d_{out_pore}} = 11.364 \frac{1}{\mu m}$$

Surface Area Enhancement for Single Nanopore:

$$SA := \pi \cdot d_{in_pore} \cdot h = 3.061 \mu m^2$$

Surface Area Enhancement for Surface:

$$SAA := \rho_{pores}^2 \cdot SA = 395.295$$

BIBLIOGRAPHY

- [1] S. V. Garimella, T. Persoons, J.A. Weibel, V. Gektin, Electronics Thermal Management in Information and Communications Technologies: Challenges and Future Directions, *IEEE Trans. Components, Packag. Manuf. Technol.* 7 (2017) 1191–1205. doi:10.1109/TCPMT.2016.2603600.
- [2] S.S.D.B.R.H.M.K.J.M.E.H.N.A.I.L.W. Shehabi Arman; Smith, United States Data Center Energy Usage Report - LBNL-1005775, (2017).
- [3] P.E. Tuma, The merits of open bath immersion cooling of datacom equipment, *Annu. IEEE Semicond. Therm. Meas. Manag. Symp.* (2010) 123–131. doi:10.1109/STHERM.2010.5444305.
- [4] F.P. Incropera, T.L. Bergman, A.S. Lavine, D.P. DeWitt, *Fundamentals of Heat and Mass Transfer.* (2011) Chapter 1: Introduction 2-67.
- [5] Fujitsu, Fujitsu Liquid Immersion Cooling System, 2017.
- [6] 3M Electronics Materials Solutions Division, Two-Phase Immersion Cooling: A revolution in data center efficiency, 2015. <https://multimedia.3m.com/mws/media/11279200/2-phase-immersion-cooling-a-revolution-in-data-center-efficiency.pdf>.
- [7] 3M Electronics Materials Solutions Division, Go for the Green - 3M immersion cooling technology helps Japanese firm take Green 500 honors, 2015. doi:10.4324/9781351008242-4.
- [8] M.S. El-Genk, H. Bostanci, Combined effects of subcooling and surface orientation on pool boiling of HFE-7100 from a simulated electronic chip, *Exp. Heat Transf.* 16 (2003) 281–301. doi:10.1080/08916150390242244.
- [9] M.S. El-Genk, H. Bostanci, Saturation boiling of HFE-7100 from a copper surface, simulating a microelectronic chip, *Int. J. Heat Mass Transf.* 46 (2003) 1841–1854. doi:10.1016/S0017-9310(02)00489-1.
- [10] A. Das, R. Ganguly, T.M. Schutzius, C.-J. Kim, A.R. Betz, C. Frankiewicz, D. Attinger, C.M. Megaridis, Surface engineering for phase change heat transfer: A review, *MRS Energy Sustain.* 1 (2014) 1–85. doi:10.1557/mre.2014.9.

- [11] A.R. Balakrishnan, R.J. Benjamin, Nucleation site density in pool boiling of saturated pure liquids: Effect of surface microroughness and surface and liquid physical properties, *Exp. Therm. Fluid Sci.* 15 (1997) 32–42.
- [12] K.H. Chu, Y.S. Joung, R. Enright, C.R. Buie, E.N. Wang, Hierarchically structured surfaces for boiling critical heat flux enhancement, *Appl. Phys. Lett.* 102 (2013) 1–5. doi:10.1063/1.4801811.
- [13] A. Majumdar, R. Chen, H.H. Cho, Z. Wang, V. Srinivasan, M.-C. Lu, Nanowires for Enhanced Boiling Heat Transfer, *Nano Lett.* 9 (2009) 548–553. doi:10.1021/nl8026857.
- [14] S. Vemuri, K.J. Kim, Pool boiling of saturated FC-72 on nano-porous surface, *Int. Commun. Heat Mass Transf.* 32 (2005) 27–31. doi:10.1016/j.icheatmasstransfer.2004.03.020.
- [15] M. Arik, A. Bar-Cohen, S.M. You, Enhancement of pool boiling critical heat flux in dielectric liquids by microporous coatings, *Int. J. Heat Mass Transf.* 50 (2007) 997–1009. doi:10.1016/j.ijheatmasstransfer.2006.08.005.
- [16] M. Vallejo, A. Siddarth, V. Mulay, D. Agonafer, J. Edward Fernandes, R. Eiland, Thermal Performance and Efficiency of a Mineral Oil Immersed Server Over Varied Environmental Operating Conditions, *J. Electron. Packag.* 139 (2017) 041005. doi:10.1115/1.4037526.
- [17] J.L. Parker, M.S. El-Genk, Pool boiling of dielectric liquids on porous graphite and extended copper surface, (2008). http://isnps.unm.edu/reports/ISNPS_Tech_Report_85.pdf.
- [18] T.M. Anderson, I. Mudawar, Microelectronic Cooling by Enhanced Pool Boiling of a Dielectric Fluorocarbon Liquid, *J. Heat Transfer.* 111 (2009) 752. doi:10.1115/1.3250747.
- [19] K.C. Leong, J.Y. Ho, K.K. Wong, A critical review of pool and flow boiling heat transfer of dielectric fluids on enhanced surfaces, *Appl. Therm. Eng.* 112 (2017) 999–1019. doi:10.1016/j.applthermaleng.2016.10.138.
- [20] S. Ujereh, T. Fisher, I. Mudawar, Effects of carbon nanotube arrays on nucleate pool boiling, *Int. J. Heat Mass Transf.* 50 (2007) 4023–4038. doi:10.1016/j.ijheatmasstransfer.2007.01.030.
- [21] W. Hou, G. Ding, W. Liu, Y. Deng, C. Ran, Wetting on Nanoporous Alumina Surface: Transition between Wenzel and Cassie States Controlled by Surface Structure, *Langmuir.* 24 (2008) 9952–9955. doi:10.1021/la801461j.

- [22] B.J. Jones, J.P. McHale, S. V. Garimella, The Influence of Surface Roughness on Nucleate Pool Boiling Heat Transfer, *J. Heat Transfer*. 131 (2009) 121009. doi:10.1115/1.3220144.
- [23] C. Young Lee, M.M. Hossain Bhuiya, K.J. Kim, Pool boiling heat transfer with nano-porous surface, *Int. J. Heat Mass Transf.* 53 (2010) 4274–4279. doi:10.1016/j.ijheatmasstransfer.2010.05.054.
- [24] D. Cooke, S.G. Kandlikar, Pool Boiling Heat Transfer and Bubble Dynamics Over Plain and Enhanced Microchannels, *J. Heat Transfer*. 133 (2011) 052902. doi:10.1115/1.4003046.
- [25] M.C. Lu, R. Chen, V. Srinivasan, V.P. Carey, A. Majumdar, Critical heat flux of pool boiling on Si nanowire array-coated surfaces, *Int. J. Heat Mass Transf.* 54 (2011) 5359–5367. doi:10.1016/j.ijheatmasstransfer.2011.08.007.
- [26] A. Kalani, S.G. Kandlikar, Pool Boiling of FC-87 Over Microchannel Surfaces At Atmospheric Pressure, in: ASME, Houston, Texas, 2012: 1–7.
- [27] D. Cooke, S.G. Kandlikar, Effect of open microchannel geometry on pool boiling enhancement, *Int. J. Heat Mass Transf.* 55 (2012) 1004–1013. doi:10.1016/j.ijheatmasstransfer.2011.10.010.
- [28] A.R. Betz, J. Jenkins, C.J. Kim, D. Attinger, Boiling heat transfer on superhydrophilic, superhydrophobic, and superbiphilic surfaces, *Int. J. Heat Mass Transf.* 57 (2013) 733–741. doi:10.1016/j.ijheatmasstransfer.2012.10.080.
- [29] M.M. Rahman, E. Ölçeroglu, M. McCarthy, Role of wickability on the critical heat flux of structured superhydrophilic surfaces, *Langmuir*. 30 (2014) 11225–11234. doi:10.1021/la5030923.
- [30] D.I. Yu, H.S. Ahn, D.E. Kim, D.W. Jerng, M.H. Kim, Review of boiling heat transfer enhancement on micro/nanostructured surfaces, *Exp. Therm. Fluid Sci.* 66 (2015) 173–196. doi:10.1016/j.expthermflusci.2015.03.023.
- [31] J. Miller, P. KC, P.A. Primeaux, W.J. Meng, X. Zhang, A.L. Moore, B. Zhang, Aluminum-based one- and two-dimensional micro fin array structures: high-throughput fabrication and heat transfer testing, *J. Micromechanics Microengineering*. 27 (2016) 025012. doi:10.1088/1361-6439/aa53c9.
- [32] H.Y. Hsu, M.C. Lin, B. Popovic, C.R. Lin, N.A. Patankar, A numerical investigation of the effect of surface wettability on the boiling curve, *PLoS One*. 12 (2017) e0187175. doi:10.1371/journal.pone.0187175.

- [33] D. Il Shim, G. Choi, N. Lee, T. Kim, B.S. Kim, H.H. Cho, Enhancement of Pool Boiling Heat Transfer Using Aligned Silicon Nanowire Arrays, *ACS Appl. Mater. Interfaces*. (2017). doi:10.1021/acsami.7b01929.
- [34] B. Lu, W.J. Meng, Roll Molding of Microchannel Arrays on Al and Cu Sheet Metals: A Method for High-Throughput Manufacturing, *J. Micro Nano-Manufacturing*. (2013). doi:10.1115/1.4025978.
- [35] J. Lee, Y. Kim, U. Jung, W. Chung, Thermal conductivity of anodized aluminum oxide layer: The effect of electrolyte and temperature, *Mater. Chem. Phys.* (2013). doi:10.1016/j.matchemphys.2013.05.058.
- [36] C.Y. Lee, B.J. Zhang, K.J. Kim, Morphological change of plain and nano-porous surfaces during boiling and its effect on nucleate pool boiling heat transfer, *Exp. Therm. Fluid Sci.* (2012). doi:10.1016/j.expthermflusci.2012.02.011.
- [37] Y.Y. Hsu, On the Size Range of Active Nucleation Cavities on a Heating Surface, *J. Heat Transfer*. (2012). doi:10.1115/1.3684339.